

Deep Ocean Temperatures through Time

Paul J Valdes¹, Christopher R Scotese², Daniel J Lunt¹

¹ School of Geographical Sciences, University of Bristol, Bristol BS8 1SS, UK

² Northwestern University, Dept Earth & Planetary Sci, Evanston, IL USA

Correspondence to: Paul Valdes (P.J.Valdes@bristol.ac.uk)

Abstract

Benthic oxygen isotope records are commonly used as a proxy for global mean surface temperatures during the late Cretaceous and Cenozoic, and the resulting estimates have been extensively used in characterising major trends and transitions in the climate system, and for analysing past climate sensitivity. However, some fundamental assumptions governing this proxy have rarely been tested. Two key assumptions are: (a) benthic foraminiferal temperatures are geographically well-mixed and are linked to surface high latitude temperatures, and (b) surface high latitude temperatures are well correlated with global mean temperatures. To investigate the robustness of these assumptions through geological time, we performed a series of 109 climate model simulations using a unique set of paleogeographical reconstructions covering the entire Phanerozoic at the stage-level. The simulations have been run for at least 5000 model years to ensure that the deep ocean is in dynamic equilibrium. We find that the correlation between deep ocean temperatures and global mean surface temperatures is good for the Cenozoic and thus the proxy data are reliable indicators for this time period, albeit with a standard error of 2K. This uncertainty has not normally been assessed and needs to be combined with other sources of uncertainty when, for instance, estimating climate sensitivity based on using $\delta^{18}\text{O}$ measurements from benthic foraminifera. The correlation between deep and global mean surface temperature becomes weaker for pre-Cenozoic time periods (when the paleogeography is significantly different than the present-day). The reasons for the weaker correlation ~~includes~~include variability in the source region of the deep water (varying hemispheres but also varying latitudes of sinking), the depth of ocean overturning (some extreme warm climates have relatively shallow and sluggish circulations weakening the link between surface and deep ocean), and the extent of polar amplification (e.g. ice albedo feedbacks). Deep ocean sediments prior to the Cretaceous are rare, so extending the benthic foram proxy further into deeper time is problematic, but the model results presented here would suggest that the ~~predicted~~ deep ocean temperatures from such time periods would probably be an unreliable indicator of global mean surface conditions.

97

98 1. Introduction

99

100 One of the most widely used proxies for estimating global mean surface temperature through the
101 last 100 million years is benthic $\delta^{18}\text{O}$ measurements from deep sea foraminifera (Zachos et al.,
102 2001), (Zachos et al., 2008), (Cramer et al., 2009), (Friedrich et al., 2012). Two key underlying
103 assumptions are that $\delta^{18}\text{O}$ from benthic foraminifera represents deep ocean temperature (with a
104 correction for ice volume effects and any vital effects), and that the deep ocean water masses
105 originate from surface water in polar regions. By further assuming that polar surface temperatures
106 are well correlated with global mean surface temperatures, then deep ocean isotopes can be
107 assumed to track global mean surface temperatures. More specifically, (Hansen et al., 2008), and
108 (Hansen and Sato, 2012) argue that changes in high latitude sea surface temperatures are
109 approximately proportional to global mean surface temperatures because changes are generally
110 amplified at high latitudes but that this is offset because temperature change is amplified over land
111 areas. They therefore equate changes in benthic ocean temperatures with global mean surface
112 temperature.

113 The resulting estimates of global mean surface air temperature have been used to understand past
114 climates (e.g. (Zachos et al., 2008), (Zachos et al., 2008), (Cramer et al., 2009), (Friedrich et al., 2012)).
115 Two key underlying assumptions are that $\delta^{18}\text{O}$ from benthic foraminifera represents deep ocean
116 temperature (with a correction for ice volume and any vital effects), and that the deep ocean water
117 masses originate from surface water in polar regions. By further assuming that polar surface
118 temperatures are well correlated with global mean surface temperatures, then deep ocean isotopes
119 can be assumed to track global mean surface temperatures. More specifically, (Hansen et al., 2008),
120 and (Hansen and Sato, 2012) argue that changes in high latitude sea surface temperatures are
121 approximately proportional to global mean surface temperatures because changes are generally
122 amplified at high latitudes but that this is offset because temperature change is amplified over land
123 areas. They therefore directly equate changes in benthic ocean temperatures with global mean
124 surface temperature.

125 The resulting estimates of global mean surface air temperature have been used to understand past
126 climates (e.g. (Zachos et al., 2008)). Combined with estimates of atmospheric CO_2 they have also
127 been used to estimate climate sensitivity (e.g. (Hansen et al., 2013)) and hence contribute to the
128 important ongoing debate about the likely magnitude of future climate change.

Formate

158 However, some of the underlying assumptions behind the method remains largely untested, even
159 though we know that there are major changes to paleogeography and consequent changes in ocean
160 circulation and location of deep-water formation in the deep past (e.g. (Lunt et al., 2010; Nunes and
161 Norris, 2006); (~~Farnsworth et al., 2019a~~); (~~Donnadieu et al., 2016~~); (~~Farnsworth et al., 2019a~~);
162 (~~Ladant et al., 2020~~)). Moreover, the magnitude of polar amplification is likely to vary depending on
163 the extent of polar ice caps, and changes in cloud cover (Sagoo et al., 2013), (Zhu et al., 2019). These
164 issues are likely to modify the correlation between deep ocean temperatures and global mean
165 surface temperature or, at the very least, increase the uncertainty in reconstructing past global
166 mean surface temperatures.

167 The aim of this paper is two fold, (1) we wish to investigate document the strength setup and
168 accuracy of the deep ocean temperature proxy using initial results from a unique set of 109 climate
169 model simulations of the whole Phanerozoic era (last 540 million years) at the stage level
170 (approximately every 5 million years). ~~We~~, and (2) we will use ~~this set of model these~~ simulations to
171 study investigate the relationship between accuracy of the deep ocean temperature ~~and proxy in~~
172 representing global mean surface temperature.

173 The focus of the work is to examine the ~~mechanisms that~~ link between benthic ocean temperatures
174 and surface conditions. However, we evaluate the fidelity of the model by comparing the model
175 predicted ocean temperatures to estimates of the isotopic temperature of the deep ocean during
176 the past 110 million years (~~(Zachos et al., 2008)~~(Zachos et al., 2008), (~~Cramer et al., 2009~~)(Cramer et
177 al., 2009), (~~Friedrich et al., 2012~~)(Friedrich et al., 2012)), and model predicted surface temperatures
178 to the sea surface temperatures estimates of (O'Brien et al., 2017) and (Cramwinckel et al., 2018).

179 This gives us confidence that the model is behaving plausibly. but we emphasise that the fidelity of
180 the simulations is strongly influenced by the accuracy of CO₂ estimates through time. We then use
181 the complete suite of climate simulations to examine changes in ocean circulation, ice formation,
182 and the impact on ocean and surface temperature. Our paper will not consider any issues associated
183 with assumptions regarding the relationship between deep-sea foraminifera $\delta^{18}\text{O}$ and various
184 temperature calibrations because our model does not simulate the $\delta^{18}\text{O}$ of sea water (or vital
185 effects).

186

219 2. Simulation Methodology

220 2.1 Model Description

221 We use a variant of the Hadley Centre model, HadCM3 (~~(Pope et al., 2000)~~(Pope et al., 2000),
222 ~~(Gordon et al., 2000)~~(Gordon et al., 2000)) which is a coupled atmosphere-ocean-vegetation model.

223 The specific version, HadCM3BL-M2.1Da1aD, is described in detail in (Valdes et al., 2017). The model
224 has a horizontal resolution of 3.75° x 2.5° in longitude/latitude (roughly corresponding to an average
225 grid box size of ~300km) in both the atmosphere and the ocean. The atmosphere has 19 unequally
226 spaced vertical levels, and the ocean has 20 unequally spaced vertical levels. Though HadCM3 is
227 relatively low resolution and low complexity model compared to the current CMIP5/CMIP6 state-of-
228 the-art model, its performance at simulating modern climate is comparable to many CMIP5 models
229 (Valdes et al., 2017). The performance of the dynamic vegetation model compared to modern
230 observations is also described in (Valdes et al., 2017) but the modern deep ocean temperatures are
231 not described in that paper. We therefore include a comparison to present day observed deep ocean
232 temperatures in section 3.1.

233 ~~In order to~~To perform paleo--simulations, several important modifications to the standard model
234 described in (Valdes et al., 2017) must be incorporated:

235 (a) The standard pre-industrial model uses a prescribed climatological pre-industrial ozone
236 concentration (i.e. prior to the development of the “ozone” hole) which is a function of
237 latitude, atmospheric height, and month of the year. However, we do not know what the
238 distribution of ozone should be in these past climates. (Beerling et al., 2011) modelled small
239 changes in tropospheric ozone for the early Eocene and Cretaceous but no comprehensive
240 stratospheric estimates are available. Hence most paleoclimate model simulations assume
241 unchanging concentrations. However, there is a problem with using a prescribed ozone
242 distribution for paleo--simulations because it does not incorporate ozone feedbacks
243 associated with changes in tropospheric height. During warm climates, the model predicts
244 that the tropopause would rise. In the real world, ozone would track the tropopause rise,
245 however, this rising ozone feedback is not included in our standard model. This leads to
246 substantial extra warming and artificially increases the apparent climate sensitivity.
247 Simulations of future climate change have shown that ozone feedbacks can lead to an over-
248 estimate of climate sensitivity by up to 20% (~~(Dietmuller et al., 2014)~~(Dietmuller et al.,
249 2014), (Nowack et al., 2015)). ~~Therefore, in order~~(Nowack et al., 2015)) (Hardiman et al.,
250 2019). Therefore, to incorporate some aspects of this feedback, we have changed the ozone

280 scheme in the model. Ozone is coupled to the model predicted tropopause height every
281 model timestep in the following simple way:

- 282 • 2.0×10^{-8} kg/kg in the troposphere
- 283 • 2.0×10^{-7} kg/kg at the tropopause
- 284 • 5.5×10^{-6} kg/kg above the tropopause
- 285 • 5.5×10^{-6} kg/kg at the top model level.

286 These values are approximate averages of present-day values and were chosen so that the
287 tropospheric climate of the resulting pre-industrial simulation was little altered compared
288 with the standard preindustrial simulations; the resulting global mean surface air
289 temperatures differed by only 0.05 °C. These modifications are similar to those used in the
290 FAMOUS model (Smith et al., 2008) except that the values in the stratosphere are greater in
291 our simulation, largely because our model vertical resolution is higher than in FAMOUS.

292 Note that these changes improve upon the scheme used by (Lunt et al., 2016). ~~They used
293 much lower values of stratospheric ozone and had no specified value at the top of the
294 model. This resulted in their model having ~ 1°C cold bias for pre-industrial temperatures.
295 This may have also affected their estimates of climate sensitivity.~~

296 and (Farnsworth et al., 2019a). They used much lower values of stratospheric ozone and
297 had no specified value at the top of the model. This resulted in their model having ~ 1°C cold
298 bias for pre-industrial temperatures and may have also affected their estimates of climate
299 sensitivity.

300 (b) The standard version of HadCM3 conserves the total volume of water throughout the
301 atmosphere and ocean (including in the numerical scheme) but several processes in the
302 model “lose or gain” water:

- 303 1. Snow accumulates over ice sheets but there is no interactive loss through iceberg
304 calving resulting in an excess loss of fresh water from the ocean.
- 305 2. The model caps salinity at a maximum of 45 PSU (and a minimum of 0 PSU), by
306 artificially adding/subtracting fresh water to the ocean. This mostly affects small
307 enclosed seas (such as the Red Sea or enclosed Arctic) where the model does not
308 represent the exchanges with other ocean basins.

- 309 3. Modelled river runoff includes some river basins which drain internally. These often
310 correspond to relatively dry regions, but any internal drainage simply disappears
311 from the model.
- 312 4. The land surface scheme includes evaporation from sub-grid scale lakes (which are
313 prescribed as a lake fraction in each grid box, at the start of the run). The model
314 does not represent the hydrological balance of these lakes, consequently the
315 volume of the lakes does not change. This effectively means that there is a net
316 source/sink of water in the model in these regions.

317 In the standard model, these water sources/sinks are approximately balanced by a flux of
318 water into the surface ocean. This is prescribed at the start of the run and does not vary
319 during the simulations. It is normally set to a pre-calculated estimate based on an old
320 HadCM3-M1 simulation. The flux is strongest around Greenland and Antarctica and is
321 chosen such that it approximately balances the water loss described in (1) i.e. the net snow
322 accumulation over these ice sheets. There is an additional flux covering the rest of the
323 surface ocean which approximately balances the water loss from the remaining three terms
324 (2-4). The addition of this water flux keeps the global mean ocean salinity approximately
325 constant on century time scales. However, depending on the simulation the drift in average
326 oceanic salinity can be as much as 1PSU per thousand years and thus can have a major
327 impact on ultra-long runs ((Farnsworth et al., 2019a). However, depending on the simulation,
328 the drift in average oceanic salinity can be as much as 1PSU per thousand years and thus can
329 have a major impact on ultra-long runs of >5000 years (Farnsworth et al., 2019a).

330 For the paleo-simulations in this paper, we therefore take a slightly different approach.
331 When ice sheets are present in the Cenozoic, we include the water flux (for the relevant
332 hemisphere) described in (1) above, based on modern values of iceberg calving fluxes for
333 each hemisphere. However, to ensure that salinity is conserved, we also interactively
334 calculate an additional globally uniform surface water flux based on relaxing the volume
335 mean ocean salinity to a prescribed value on a 20-year timescale. This ensures that there is
336 no long-term trend in ocean salinity. Tests of this update on the pre-industrial simulations
337 revealed no appreciable impact on the skill of the model relative to the observations. We
338 have not directly compared our simulations to the previous runs of the (Farnsworth et al.,
339 2019a) because they use different CO₂ and different paleogeographies. However in practice,
340 the increase of salinity in their simulations is well mixed and seems to have relatively little
341 impact on the overall climate and ocean circulation.

We have little knowledge of whether ocean salinity has changed through time, and so keep the prescribed mean ocean salinity constant across all simulations.

2.2 Model Boundary Conditions

There are several boundary conditions that require modification through time. In this sequence of simulations, we only modify three key time-dependent boundary conditions: 1) the solar constant, 2) atmospheric CO₂ concentrations and, 3) paleogeographic reconstructions. We set the surface soil conditions to a uniform medium loam everywhere. All other boundary conditions (such as orbital parameters, volcanic aerosol concentrations etc.) are held constant at pre-industrial values.

The solar constant is based on ~~(Gough, 1981)~~(Gough, 1981) and increases linearly at an approximate rate of 11.1 Wm⁻² per 100 Ma (0.8% per 100Ma), to 1365Wm⁻² currently. If we assume a planetary albedo of 0.3, and a climate sensitivity of 0.8 °C /Wm⁻² (approximately equivalent to 3°C per doubling of CO₂), then this is equivalent to a temperature increase of ~.015°C per million years ~~(8.1°C)~~(~8°C) over the whole of the Phanerozoic).

Estimates of atmospheric CO₂ concentrations have considerable uncertainty. We, therefore, use two alternative estimates (fig. 1a). The first uses the best fit Loess curve from ~~(Foster et al., 2017)~~(Foster et al., 2017), which is also very similar to the newer data from (Witkowski et al., 2018). The CO₂ levels have considerable short and long-term variability throughout the time period. ~~TheOur~~ second ~~curveestimate~~ removes much of the shorter term variability in the Foster (2017) curve. It was ~~used~~developed for two reasons. Firstly, a lot of the finer temporal structure in the Loess curve is a product of ~~different sampling numbers~~differing data density of the raw data and does not necessarily correspond to real features. Secondly, the smoother curve was heavily influenced by a previous (commercially confidential) sparser sequence of simulations using non-public paleogeographic reconstructions ~~and which were~~. The resulting simulations were generally in good agreement with terrestrial proxy datasets (Harris et al., 2017). Specifically, using commercial in confidence paleogeographies, we have performed multiple simulations at different CO₂ values for several stages across the last 440 million years and tested the resulting climate against commercial-in-confidence proxy data (Harris et al., 2017). We then selected the CO₂ that best matched the data. For the current simulations, we linearly interpolated these CO₂ values to every stage. The resulting CO₂ curve looks like a heavily smoothed version of the Foster curve and is within the (large) envelope of CO₂ reconstructions. The first-order shapes of the two curves are similar, though they are very different for some time periods (e.g. Triassic and Jurassic). ~~Both~~In practice, both curves

Formatted

439 ~~largely sit within~~ should be considered an approximation to the range of actual data points. ~~evolution~~
440 of CO₂ through time which remains uncertain.

441 We refer to the simulation using the second set of CO₂ reconstructions as the “smooth” CO₂
442 simulations, though it should be recognised that the Foster CO₂ curve has also been smoothed. The
443 Foster CO₂ curve extends ~~only~~ back to only 420 Ma, so we have proposed two alternative extensions
444 back to 540 Ma. Both curves increase sharply so that the combined forcing of CO₂ and solar
445 constant are approximately constant over this time period ~~(Foster et al., 2017).~~ (Foster et al., 2017).
446 The higher CO₂ in the Foster curve relative to the “smooth” curve is because the initial ~~set of~~
447 simulations showed that the Cambrian simulations were relatively cool compared to data estimates
448 for the period (Henkes et al., 2018).

449 2.3 Paleogeographic Reconstructions

450 The 109 paleogeographic maps used in the HadleyCM3 simulations are digital representations of the
451 maps in the PALEOMAP Paleogeographic Atlas ~~(Scotese, 2016); (Scotese and Wright, 2018)~~ (Scotese,
452 2016); (Scotese and Wright, 2018). Table 1 lists all the time intervals that comprise the PALEOMAP
453 Paleogeographic Atlas. The PaleoAtlas contains one map for nearly every stage in the Phanerozoic.
454 A paleogeographic map is defined as a map that shows the ancient configuration of the ocean basins
455 and continents, as well as important topographic and bathymetric features such as mountains,
456 lowlands, shallow sea, continental shelves, and deep oceans. Paleogeographic reconstructions older
457 than the oldest ocean floor (~Late-Jurassic) have uniform deep ocean floor depth.

458 Once the paleogeography for each time interval has been mapped, this information is then
459 converted into a digital representation of the paleotopography and paleobathymetry. Each digital
460 paleogeographic model is composed of over 6 million grid cells that capture digital elevation
461 information at a 10 km x 10 km horizontal resolution and 40-meter vertical resolution. This
462 quantitative, paleo-digital elevation model, or “paleoDEM”, allows us to visualize and ~~analyze~~
463 the changing surface of the Earth through time using GIS software and other computer modeling
464 techniques. For use with the HadCM3L climate model, the original high-resolution elevation grid was
465 reduced to a ~111 km x ~111 km (1° x 1°) grid.

466 For a detailed description of how the paleogeographic maps and paleoDEMs were produced the
467 reader is referred to ~~(Scotese, 2016); (Scotese and Schettino, 2017); (Scotese and Wright, 2018).~~
468 ~~(Scotese and Schettino, 2017) includes an annotated bibliography of the more than 100 key sources~~
469 ~~of paleogeographic information. Similar paleogeographic paleoDEMs have been produced by~~
470 ~~(Baatsen et al., 2016)~~ (Scotese, 2016); (Scotese and Schettino, 2017); (Scotese and Wright, 2018).
471 ~~(Scotese and Schettino, 2017) includes an annotated bibliography of the more than 100 key sources~~

505 of paleogeographic information. Similar paleogeographic paleoDEMs have been produced by
506 (Baatsen et al., 2016) and (Verard et al., 2015).

507 The raw paleogeographic data reconstructs paleo-elevations and paleo-bathymetry at a resolution of
508 $1^\circ \times 1^\circ$. These data were re-gridded to $3.75^\circ \times 2.5^\circ$ resolution that matched the GCM using a simple
509 area (for land sea mask) or volume (for orography and bathymetry) conserving algorithm. The
510 bathymetry was lightly smoothed (using a binomial filter) to ensure that the ocean properties in the
511 resulting model simulations were numerically stable. The high latitudes had this filter applied
512 multiple times. The gridding sometimes produced single grid point enclosed ocean basins,
513 particularly along complicated coastlines, and these were manually removed. Similarly, important
514 ocean gateways were reviewed to ensure that the re-gridded coastlines preserved these structures.
515 The resulting global fraction of land is summarized in fig.1b and examples are shown in figure 2. The
516 original reconstructions can be found at [https://www.earthbyte.org/paleodem-resource-scotese-](https://www.earthbyte.org/paleodem-resource-scotese-and-wright-2018/)
517 and-wright-2018/. Maps of each HadCM3L paleogeography are included in the supplementary
518 figures.

519 The paleogeographic reconstructions also include an estimate of land ice area (~~(Scotese and Wright,~~
520 ~~2018)~~(Scotese and Wright, 2018); fig.1c). These were converted to GCM boundary conditions
521 assuming a simple parabolic shape to estimate the ice sheet height. ~~Unlike (Lunt et al., 2016),~~
522 ~~these~~These ice reconstructions suggest small amounts of land ice were present during the early
523 Cretaceous, unlike (Lunt et al., 2016) who used ice-free Cretaceous paleogeographies.

524 2.4 Spin up Methodology

525 The oceans are the slowest evolving part of the modelled climate system and can take multiple
526 millennia to reach equilibrium, depending on the initial condition and climate state. ~~In order to~~To
527 speed up the convergence of the model, we initialized the ocean temperatures and salinity with the
528 values from previous model simulations from similar time periods. The atmosphere variables were
529 initialized in a similar manner.

530 Simulations were run in parallel so were not initialised from the previous stage results using these
531 paleogeographies. In total, we performed almost 1 million years of model simulation and if we ran
532 simulations in sequence, it would have taken 30 years to complete the simulations. By running these
533 in parallel, initialised from previous modelling studies, we reduced the total run time to 3 months,
534 albeit using a substantial amount of our high performance computer resources.

535 Although it is always possible that a different initialization procedure may produce different final
536 states, ~~our experience is that the HadCM3 and HadCM3L have rarely shown multiple equilibria. it is~~
537 impossible to explore the possibility of hysteresis/bistability without performing many simulations

538 for each period, which is currently beyond our computing resources. Previous studies using
539 HadCM3L (not published) with alternative ocean initial states (isothermal at 0C, 8C, and 16C) have
540 not revealed multiple equilibria but this might have been because we did not locate the appropriate
541 part of parameter space that exhibits hysteresis. However, other studies have shown such behaviour
542 (e.g. (Baatsen et al., 2018)). This remains a caveat of our current work and which we wish to
543 investigate when we have sufficient computing resource.

544 The simulations were then run until they reached equilibrium, as defined by:

- 545 1. The globally and volume integrated annual mean ocean temperature trend is less than
546 1°C/1000 year, in most cases considerably smaller than this. We consider the volume
547 integrated temperature because it includes all aspects of the ocean. However, it is
548 dominated by the deep ocean trends and is near identical to the trends at a depth of 2731m
549 (the lowest level that we have archived for the whole simulation).
- 550 2. The trends in surface air temperature are less than 0.3°C/1000 year
- 551 3. The net energy balance at the top of the atmosphere, averaged over 100-year period at the
552 end of the simulation, is less than 0.25 Wm⁻² (in more than 80% of the simulations, the
553 imbalance is less than 0.1 Wm⁻²). The Gregory plot ~~(Gregory et al., 2004)~~(Gregory et al.,
554 2004) implies surface temperatures are within 0.3°C of the equilibrium state.

555 These target trends ~~were~~ chosen ~~because they were somewhat arbitrary but~~ are all less than typical
556 orbital time scale variability (e.g. temperature changes since the last deglaciation were
557 approximately 5°C over 10,000 years). Most simulations were well within these criteria. 70% of
558 simulations had residual net energy balances at the top of the atmosphere of less than 0.1 Wm⁻², but
559 a few simulations were slower to reach full equilibrium. The strength of using multiple constraints is
560 that a simulation may, by chance, pass one or two of these criteria but were unlikely to pass all three
561 tests. For example, all the models that we extended failed at least two of the criteria. The resulting
562 time series of volume integrated global, annual mean ocean temperatures are shown in fig. 3. The
563 supplementary figures also include this for each simulation, as well as the trends at 2731m.

564 The “smooth” CO₂ simulations were all run for ~~5000~~5050 model years and satisfied the criteria. The
565 Foster-CO₂ simulations were initially run for a minimum of 2000 years, (starting from the end of the
566 5000 year runs), at which point we reviewed the simulations relative to the convergence criteria. If
567 the simulations had not converged, we extended the runs for an additional 3000 years. If they had
568 not converged at the end of 5000 years, we extended them again for an additional 3000 years. After
569 8000 years, all simulations had converged based on the convergence criteria. In general, the slowest
570 converging simulations corresponded to some of the warmest climates (final temperatures in figure

576 3b and 3c were generally warmer than in figure 3a) ~~and almost all had significantly different final~~
577 ~~climates compared to their initialization). It cannot be guaranteed that further changes will not~~
578 ~~occur; however, we note that the criteria and length of the simulations greatly exceed PMIP-LGM~~
579 ~~(Kageyama et al., 2017) and PMIP-DeepMIP (Lunt et al., 2017) protocols.~~

580

Formate

613 3. Results

614 3.1 Comparison of Deep Ocean Temperatures to Benthic Ocean Data

615 Before using the model to investigate the linkage of deep ocean temperatures to global mean
616 surface temperatures, it is interesting to evaluate whether the modelled deep ocean temperatures
617 agree with the deep ocean temperatures obtained from the isotopic studies of benthic foraminifera
618 (Friedrich et al., 2012; Zachos et al., 2008). It is important to note that the temperatures are ~~likely to~~
619 ~~be~~ strongly influenced by the choice of CO₂, so we are not ~~necessarily seeking perfect~~ expecting
620 complete agreement, but we simply wish to evaluate whether the model is within a plausible ~~range~~-
621 ranges. If the modelled temperatures were in complete disagreement with data, then it might
622 suggest that the model was too far away from reality to allow us to adequately discuss deep
623 ocean/surface ocean linkages. If the modelled temperatures are plausible, then it shows that we are
624 operating within the correct climate space. A detailed comparison of modelled surface and benthic
625 temperatures to data throughout the Phanerozoic, using multiple CO₂ scenarios, is the subject of a
626 separate ongoing project.

627 Figure 4a compares the modelled deep ocean temperature to the foraminifera data from the
628 Cenozoic and Cretaceous (115 Ma). The observed isotope data are converted to deep ocean
629 temperature using the procedures described by (Hansen et al., 2013). The modelled deep
630 temperature shown in fig.4a (solid line) is the average temperature at the bottom level of the model,
631 excluding depths less than 1000m (to avoid continental shelf locations which are typically not
632 included in benthic data compilations). The observed benthic data are collected from a range of
633 depths and are rarely at the very deepest levels (e.g. the new cores in (Friedrich et al., 2011) range
634 from current water depths ranging from 1899m to 3192m). Furthermore, large data compilations
635 rarely include how the depth of a particular site changed with time, and thus effectively assume that
636 any differences between basins and through time are entirely due to climate change and not to
637 changes in depth. Hence throughout the rest of the paper we frequently use the modelled 2731m
638 temperatures as a surrogate for the true benthic temperature. This is a pragmatic definition because
639 the area of deep ocean reduces rapidly (e.g. there is typically only 50% of the globe deeper than
640 3300m). To evaluate whether this procedure gave a reasonable result, we also calculated the global
641 average temperature at the model level at a depth of 2731m. This is shown by the dashed line in
642 figure 4a. In general, the agreement between model bottom water temperatures and 2731m
643 temperatures is very good. The standard deviation between model bottom water and constant
644 depth of 2731m is 0.7°C, and the maximum difference is 1.4°C. Compared to the overall variability,

678 this is a relatively small difference and shows that it is reasonable to assume that the deep ocean has
679 weak vertical gradients.

680 ~~The modelled deep temperature shown in fig.4a (solid line) is the average temperature at the~~
681 ~~bottom level of the model, excluding depths less than 1000m. The observed data was collected from~~
682 ~~a range of depths—including mid-ocean ridges whose depth can vary from 2000m to the true~~
683 ~~bottom of the ocean. To evaluate whether this procedure gave a reasonable result, we also~~
684 ~~calculated the global average temperature at the model layer depth closest to 2km (2116m). This is~~
685 ~~shown by the dashed line in figure 4a. In general, the agreement between model bottom water~~
686 ~~temperatures and 2km temperatures is very good. The standard deviation is 0.8°C, and the~~
687 ~~maximum difference is 1.6°C. Compared to the overall variability, this is a relatively small difference.~~

688 The total change in benthic temperatures over the late Cretaceous and Cenozoic is well reproduced
689 by the model, with the temperatures associated with the “smooth” CO₂ record being particularly
690 good. We do not expect the model to represent sub-stage changes (100,000’s of years) such as the
691 PETM excursion or OAEs, but we do expect that the broader temperature patterns should be
692 simulated.

693 Comparison of the two simulations illustrates how strongly CO₂ controls global mean temperature.
694 The Foster-CO₂ driven simulation substantially differs from the estimates of deep-sea temperature
695 obtained from benthic forams and is generally a poorer fit to data. The greatest mismatch between
696 the Foster curve and the benthic temperature curve is during the late Cretaceous and early
697 Paleogene. Both dips in the Foster-CO₂ simulations correspond to relatively low estimates of CO₂
698 concentrations. This is because For these periods, the dominant source of CO₂ values for these
699 periods is from paleosols (fig.1), which and thus we are ~~often lower than other proxies reliant on~~
700 one proxy methodology. Unfortunately, the alternative CO₂ reconstructions of (Witkowski et al.,
701 2018) have a data gap during this period.

702 A second big difference between the Foster curve and the benthic temperature curve occurs during
703 the Cenomanian-Turonian. This difference is similarly driven by a low estimate of CO₂ in the Foster-
704 CO₂ curve. These low CO₂ values are primarily based on stomatal density indices. Stomatal As can be
705 seen in figure 1, stomatal indices ~~also~~ frequently suggest CO₂ levels lower than estimates obtained
706 by other methods. The CO₂ estimates by (Witkowski et al., 2018) generally supports the higher levels
707 of CO₂ (near to 1000 ppmv) that are suggested by the “smooth” CO₂ curve.

708 Both sets of simulations underestimate the warming during the middle Miocene. ~~This issue has been~~
709 ~~seen before in other models (You et al., 2009). In order to simulate the surface warmth of the middle~~
710 ~~Miocene (15 Ma), CO₂ concentrations in the range 460–580 ppmv were required, whereas the CO₂~~

745 reconstructions for this period (Foster et al., 2017; Witkowski et al., 2018) are generally quite low
746 (250–400ppmv). This problem may be either due to the climate models having too low a climate
747 sensitivity or that the estimates of CO₂ are too low. It could also be related to a breakdown in the
748 relationship between temperatures and δ¹⁸O of benthic forams. This issue has been seen before in
749 other models e.g. (You et al., 2009), (Knorr et al., 2011), (Krapp and Jungclaus, 2011) (Goldner et al.,
750 2014) (Steinhorsdottir, 2021). In order to simulate the surface warmth of the middle Miocene (15
751 Ma), CO₂ concentrations in the range 460–580 ppmv were required, whereas the CO₂
752 reconstructions for this period (Foster et al., 2017) are generally quite low (250–400ppmv). This
753 problem may be either due to the climate models having too low a climate sensitivity or that the
754 estimates of CO₂ are too low (Stoll et al., 2019).

755 The original compilation of (Zachos et al., 2008)The original compilation of (Zachos et al., 2008)
756 represented a relatively small portion of the global ocean and the implicit assumption was made
757 that these results represented the entire ocean basin. (Cramer et al., 2009)(Cramer et al., 2009)
758 examined the data from an ocean basin perspective and suggested that these inter-basin differences
759 were generally small during the Late Cretaceous and early Paleogene (90Ma – 35 Ma) and the
760 differences between ocean basins were larger during the late Paleogene and early Neogene. Our
761 model largely also reproduces this pattern. Figure 5 shows the ocean temperature at ~~21162731~~ m
762 during the late Cretaceous (69 Ma), the late Eocene (39 Ma) and the Oligocene (31 Ma) for the
763 “smooth”-CO₂ simulations. In the late Cretaceous, the model temperatures are almost identical in
764 the North Atlantic and Pacific (8°C – 10°C). There is warmer deep water forming in the Indian Ocean
765 (deep mixed layer depths, not shown), off the West coast of Australia (10°C – 12°C), but otherwise
766 the pattern is very homogeneous. This is in agreement with some paleo
767 reconstructions paleoreconstructions for the Cretaceous (e.g. (Murphy and Thomas, 2012).(Murphy
768 and Thomas, 2012)).

769 By the time we reach the late Eocene (39 Ma), the North Atlantic and Pacific remain very similar but
770 cooler deep water (6°C – 8°C) is now originating in the South Atlantic. The South Atlantic cool
771 bottom water source remains in the Oligocene, but we see a strong transition in the North Atlantic
772 to an essentially modern circulation with the major source of deep, cold water occurring in the high
773 southerly latitudes (3°C – 5°C) and strong gradient between the North Atlantic and Pacific.

774 Figure 5 also shows the modelled deep ocean temperatures for present day (Fig. 5d) compared to
775 the World Ocean Atlas Data (fig. 5e). It can be seen that the broad patterns are well reproduced in
776 the model, with good predictions of the mean temperature of the Pacific. The model is somewhat
777 too warm in the Atlantic itself, and has a stronger plume from the Mediterranean than is shown in
778 the observations.

812

813 3.2 Comparison of Model Sea Surface Temperature to Proxy Data

Formatt

814 The previous section focused on benthic temperatures, but it is also important to evaluate whether
815 the modelled sea surface temperatures are plausible (within the uncertainties of the CO₂
816 reconstructions). Figure 4b shows a comparison between the model simulations of sea surface
817 temperature and two published synthesis of proxy SST data. (O'Brien et al., 2017) compiled TEX₈₆
818 and δ¹⁸O for the Cretaceous, separated into tropical and high-latitude (polewards of 48°) regions.
819 (Cramwinckel et al., 2018) compiled early Cenozoic tropical SST data, using Tex₈₆, δ¹⁸O, Mg/Ca and
820 clumped isotopes. We compare these to modelled SST for the region 15°S to 15°N, and for the
821 average of Northern and Southern hemispheres between 47.5° and 60°. The proxy data includes
822 sites from all ocean basins and so we also examined the spatial variability within the model. This
823 spatial variability consists of changes along longitude (effectively different ocean basins) and
824 changes with latitude (related to the gradient between equator and pole). We therefore calculated
825 the average standard deviation of SST relative to the zonal mean at each latitude (this is shown by
826 the smaller tick marks) and the total standard deviation of SST relative to the regional average. In
827 practice, the equatorial values are dominated by inter-basin variations and hence the two measures
828 of spatial variability are almost identical. The high latitude variability has a bigger difference
829 between the longitudinal variations and the total variability, because the equator-to-pole
830 temperature gradient (i.e. the temperatures at the latitude limits of the region are a few degrees
831 warmer/colder than the average). The spatial variability was very similar for the “smooth”-CO₂ and
832 Foster-CO₂ simulations so, for clarity, on figure 4b we only show the results as error bars on the
833 model Foster-CO₂ simulations.

834 Overall, the comparison between model and data is generally reasonable. The modelled equatorial
835 temperatures largely follow the data, albeit with considerable scatter in the data. Both simulations
836 tend to be towards the warmest equatorial data in the early Cretaceous (Albian). These
837 temperatures largely come from Tex₈₆ data. There are many δ¹⁸O based SST which are significantly
838 colder during this period. This data almost exclusively comes from cores 1050/1052 which are in the
839 Gulf of Mexico. It is possible that these data are offset due to a bias in the δ¹⁸O of sea water because
840 of the relatively enclosed region. The Foster-CO₂ simulations are noticeably colder than the data at
841 the Cenomanian peak warmth, which is presumably related to the relatively low CO₂ as discussed for
842 the benthic temperatures. The benthic record also showed a cool (low CO₂) bias in the late
843 Cretaceous. This is not such an obvious feature of the surface temperatures. The Foster simulations
844 are colder than the “smooth”-CO₂ simulations during the late Cretaceous but there is not a strong

877 mismatch between model and data. Both simulations are close to the observations, though the
878 “smooth”-CO₂ simulations better matches the high-latitude data (but is slightly poorer with the
879 tropical data).

880 The biggest area of disagreement between ~~modemodel~~ and data is at ~~the~~ high latitudes in the mid-
881 Cretaceous warm period. ~~As expected,~~In common with previous work with this model in the context
882 of the Eocene (Lunt et al., 2021) the model is considerably cooler than the data, with a 10-15°C
883 mismatch between models and data. ~~If we assume that the data has~~The polar sea surface
884 temperature estimates may have a seasonal bias, ~~and~~ because productivity is likely to be higher
885 during the warmer summer months and, if we select the summer ~~seasons~~season temperatures from
886 the model, then the mismatch is slightly reduced by about 4°C. The problem of a cool high latitudes
887 in models is seen in many model studies and there is increasing evidence that this is related to the
888 way that the models simulate clouds (~~(Kiehl and Shields, 2013); (Sagoo et al., Kiehl and Shields,~~
889 ~~2013); (Zhu et al., 2019)).~~
890 ; (Sagoo et al., 2013); (Upchurch et al., 2015; Zhu et al., 2019)). Of course, in practice deep water is
891 formed during winter so the benthic temperatures do not suffer from a summer bias.

892 3.3 Correlation of Deep Ocean Temperatures to Polar Sea Surface Temperatures

893 The previous sections showed that that the climate model was producing a plausible reconstruction
894 of past ocean temperature changes, at least within the uncertainties of the CO₂ estimates. We now
895 use the HadCM3L model to investigate the links between deep ocean temperature and global mean
896 surface temperature.

897 In theory, the deep ocean temperature should be correlated with the sea surface temperature at the
898 location of deep-water formation which is normally assumed to be high latitude surface waters in
899 winter. We therefore compare deep ocean temperatures (defined as the average temperature at the
900 bottom of the model ocean, where the bottom must be deeper than 1000 m) with the average
901 winter sea surface temperature polewards of 60° (fig. 6). Winter is defined as December, January,
902 and February in the northern hemisphere and June, July, and August in the southern hemisphere.
903 Also shown in Figure 6 is the best fit line, which has a slope of 0.40 (+/-0.05 at the 97.5% level), an r²
904 of 0.59, and a standard error of 1.2°C. We obtained very similar results when we compared the polar
905 sea surface temperatures with the average temperature at 2116m instead of the true benthic
906 temperatures. We also compared the deep ocean temperatures to the mean polar sea surface
907 temperatures when the mixed layer depth exceeded 250 m (poleward of 50°). The results were
908 similar although the scatter was somewhat larger (r²=0.48).

Formatted
single, S
Formatted

909 Overall, the relationship between deep ocean temperatures and polar sea surface temperatures is
910 clear (Figure 6) but there is considerable scatter around the best fit line, especially at the high end,
911 and the slope is less steep than perhaps would be expected (~~Hansen and Sato, 2012~~)(Hansen and
912 Sato, 2012). The scatter is less for the Cenozoic and late Cretaceous (up to 100 Ma; green and
913 orange dots and triangles). If we used only Cenozoic and late Cretaceous simulations, then the slope
914 is similar (0.43) but $r^2=0.92$ and standard error=0.47°C. This provides strong confirmation that
915 benthic data is a robust approximation to polar surface temperatures when the continental
916 configuration is similar to the present.

917 However, the scatter is greater for older time periods, with the largest divergence observed for the
918 warm periods of the Triassic and early Jurassic, particularly for the Foster CO₂ simulations (purple
919 and blue dots). Examination of climate models for these time periods reveals relatively sluggish and
920 shallow ocean circulation-, with weak horizontal temperature gradients at depth (though salinity
921 gradients can still be important, (Zhou et al., 2008)). For instance, in the Ladinian stage, mid-Triassic
922 (~240Ma) the overturning circulation is extremely weak (Fig. 7). The maximum strength of the
923 northern hemisphere overturning cell is less than 10 Sv and the southern cell is less than 5 Sv. Under
924 these conditions, deep ocean water does not always form at polar latitudes. Examination of the
925 mixed layer depth (not shown) shows that during these time periods, the deepest mixed layer
926 depths are in the sub-tropics. In subtropics, there is very high evaporation relative to precipitation
927 (due to the low precipitation and high temperature. This produces highly saline waters that sink and
928 spread out into the global ocean.

929 This mechanism has been previously suggested as a mechanism for warm Cretaceous deep water
930 formation (~~Brass et al., 1982~~)(Brass et al., 1982), (~~Kennett and Stott, 1991~~)(Kennett and Stott, 1991).
931 The idea that deep water may form in the tropics is in disagreement with early hypothesis (e.g.
932 (Emiliani, 1954)) but they were only considering the Tertiary and our model does not simulate any
933 low latitude deep water formation during this period. We only see significant tropical deep water
934 formation for earlier periods, and this has previously been suggested as a mechanism for warm
935 Cretaceous deep water formation (Brass et al., 1982). Deep water typically forms in convective
936 plumes. They showed that the depth and spreading of these plumes is related to the buoyancy flux
937 with the greatest flux leading to bottom water and plumes of lesser flux leading to intermediate
938 water. (Brass et al., 1982) suggested that this could occur in warm conditions in the tropics,
939 particularly if there was significant epicontinental seaways and hypothesised that it “has been a
940 dominant mechanism of deep water formation in historical times”. It is caused by a strong buoyancy
941 flux linked to strong evaporation at high temperatures.

942

943 Our computer model simulations are partly consistent with this hypothesis. The key aspect for the
944 model is a relatively enclosed seaway in the tropics and warm conditions. The paleogeographic
945 reconstructions (see supplementary figures) suggest an enclosed Tethyan-like seaway starting in the
946 Carboniferous and extending through to the Jurassic and early Cretaceous. However, the colder
947 conditions of the Carboniferous prevents strong tropical buoyancy fluxes. However, when we get
948 into the Triassic and Jurassic, the warmer conditions lead to strong evaporation at low latitudes and
949 bottom water formation in the tropics. This also explains why we see more tropical deep water (and
950 hence poorer correlations between deep and polar surface temperatures in figure 6) when using the
951 Foster CO₂ since this is generally higher (and hence warmer) than the smoothed record.

952

953 An example of the formation of tropical deep water is shown in fig. 8. This shows a vertical cross-
954 section of temperature and salinity near the equator for the Ladinian stage, mid-Triassic (240Ma).
955 The salinity and temperature cross-section clearly shows high salinity warm waters sinking to the
956 bottom of the ocean and spreading out. This is further confirmed by the water age tracer, fig. 9. This
957 shows the water age (measured as time since it experienced surface conditions, see (England, 1995))
958 at 2731m in the model for the Permian, Triassic, Cretaceous and present day. The present day
959 simulation shows that the youngest water is in the N. Atlantic and off the coast of Antarctica,
960 indicating that this is where the deep water is forming. By contrast, the Triassic period shows that
961 the youngest water is in the tropical Tethyan region and that it spreads out from there to fill the rest
962 of the ocean basin. There is no young water at high latitudes, confirming that the source of bottom
963 water is tropical only. For the Permian, although there continues to be a Tethyan-like tropical
964 seaway, the colder conditions mean that deep water is again forming at high latitudes only. The
965 Cretaceous is more complicated. It shows younger water in the high latitudes, but also shows some
966 young water in the Tethys which merges with the high latitude waters. Additional indicator of the
967 transitional nature of the Cretaceous are the mixed layer depth (see supplementary figures). This is
968 a measure of where water is mixing to deeper levels. For this time period, there are regions of deep
969 mixed layer in both the tropics and high latitudes, whereas it is only deep in the tropics for the
970 Triassic and at high latitudes for present day.

971

972 This mechanism for warm deep water formation has also been seen in other climate models (e.g.
973 (Poulsen et al., 2001)). Though it is not a pre-requisite for warm deep water formation and is thus,
974 potentially,(Barron and Peterson, 1990)). However, (Poulsen et al., 2001) conclude that in his model
975 of the Cretaceous high-latitudes sources of deep water diminish with elevated CO₂ concentrations

1009 but did not see the dominance of tropical sources. Other models (e.g. (Ladant et al., 2020)) do not
1010 show any significant tropical deep water formation, suggesting that this feature is potentially a
1011 model-dependent result.

1012 The correlation between deep ocean temperatures and the temperature of polar surface waters
1013 differs between the “smooth” CO₂ simulations and the Foster CO₂ simulations. The slope is only 0.30
1014 ($r^2=0.57$) for the “smooth” CO₂ simulations whereas the slope is 0.48 ($r^2=0.65$) for the Foster
1015 simulations. This is because CO₂ is a strong forcing agent that influences both the surface and deep
1016 ocean temperatures. By contrast, if the CO₂ does not vary as much, then the temperature does not
1017 vary as much, and the influence of paleogeography becomes more important. These
1018 paleogeographic changes generally cause subtle and complicated changes in ocean circulation that
1019 affect the location and latitude of deep-water formation.

1020 In contrast, the mid-Cretaceous is also very warm but the continental configuration (specifically, land
1021 at high southern latitudes) favoursfavours the formation of cool, high latitude deep water.

1022 Throughout the Cretaceous there is significant southern high latitude source of deep water and
1023 hence deep-water temperatures are well correlated with surface high latitude temperatures. The
1024 strength of this connection, however, may be over exaggerated in the model. Like many climate
1025 models, HadCM3 underestimates the reduction in the pole-to-Equator sea surface temperature-
1026 (Lunt et al., 2012), (Lunt et al., 2021). This means that during the Cretaceous the high latitudes are
1027 probably too cold. Consequently, some seasonal sea ice does form which encourages the formation
1028 of cold deep-water, via brine rejection.

1029 In the late Eocene (~40 Ma), the ocean circulation is similar to the Cretaceous, but the strong
1030 southern overturning cell is closer to the South Pole, indicating that the main source of deep water
1031 has moved further polewards. The poleward movement of the region of downwelling waters
1032 explains some of the variability between deep ocean temperatures and temperature of polar surface
1033 waters.

1034 For reference, we also include the present-day meridional circulation. The modern southern
1035 hemisphere circulation is essentially a strengthening of late Eocene meridional circulation. The
1036 Northern hemisphere is dominated by the Atlantic meridional overturning circulation. The Atlantic
1037 circulation pattern does not resemble the modern pattern of circulation until the Miocene.

1038 3.4 Surface Polar Amplification

1039
1040 The conceptual model used to connect benthic ocean temperatures to global mean surface
1041 temperatures assumes that there is a constant relationship between high latitude sea surface

1076 temperatures and global mean annual mean surface air temperature. ~~(Hansen and Sato,~~
1077 ~~2012)~~(Hansen and Sato, 2012) argue that this amplification is partly related to ice-albedo feedback
1078 but also includes a factor related to the contrasting amplification of temperatures on land compared
1079 to the ocean. To investigate the stability of this relationship, fig. 810 shows the correlation between
1080 polar winter sea surface temperatures (60° - 90°) and global mean surface air temperature. The
1081 polar temperatures are the average of the two winter hemispheres (i.e. average of DJF polar SSTs in
1082 the Northern hemisphere and JJA polar SSTs in the Southern hemisphere). Also shown is a simple
1083 linear regression, with an average slope of 1.3 and with an $r^2 = 0.79$. If we only use Northern polar
1084 winter temperatures, the slope is 1.1; if we only use Southern polar winter temperatures, then the
1085 slope is 0.7. Taken separately, the scatter about the mean is considerably larger (r^2 of 0.5 and 0.6
1086 respectively) than the scatter if both data sets are combined ($r^2 = 0.79$). The difference between the
1087 southern and northern hemisphere response complicates the interpretation of the proxies and leads
1088 to potentially substantial uncertainties.

1089 As expected, there appears to be a strong non-linear component to the correlation. There are two
1090 separate regimes: 1) one with a steeper slope during colder periods (average polar winter
1091 temperature less than about 1°C), and 2) a shallower slope for warmer conditions. This is strongly
1092 linked to the extent of sea-ice cover. Cooler periods promote the growth of sea-ice which
1093 strengthens the ice-albedo feedback mechanism resulting in a steeper overall temperature gradient
1094 (strong polar amplification). Of course, the ocean sea surface temperatures are constrained to be -
1095 2°C but an expansion of seaice moves this further equatorward. Conversely, the warmer conditions
1096 result in less sea ice and hence a weaker sea ice-albedo feedback resulting in a weaker temperature
1097 gradient (reduced polar amplification).

1098 Examining the Foster CO₂ and “smooth” CO₂ simulations reveals an additional factor. If we examine
1099 the “smooth” CO₂ simulations only, then the best fit linear slope is slightly less than the average
1100 slope (1.1 vs 1.3). This can be explained by the fact that we have fewer very cold climates
1101 (particularly in the Carboniferous) due to the relatively elevated levels of CO₂. However, the scatter
1102 in the “smooth” CO₂ correlation is much larger, with an r^2 of only 0.66. By comparison, correlation
1103 between Global Mean Surface Temperature and Polar Sea Surface Temperature using the Foster CO₂
1104 has a similar overall slope to the combined set and a smaller amount of scatter. This suggests that
1105 CO₂ forcing and polar amplitude forcing have an important impact on the relationship between
1106 global and polar temperatures. The variations of carbon dioxide in the Foster set of simulations are
1107 large and they drive large changes in global mean temperature. Conversely significant sea-ice albedo
1108 feedbacks characterize times when the polar amplification is important. There are several well
1109 studied processes that lead to such changes, including albedo effects from changing ice but also

Formate

Formate

1143 from poleward heat transport changes, cloud cover, and latent heat effects ((Alexeev et al., 2005;
1144 Holland and Bitz, 2003; Sutton et al., 2007)). By contrast, the “smooth” CO₂ simulations have
1145 considerably less forcing due to CO₂ variability which leads to a larger paleogeographic effect. For
1146 instance, when there is more land at the poles, there will be more evaporation over the land areas
1147 and hence simple surface energy balance arguments would suggest different temperatures ((Sutton
1148 et al., 2007)(Sutton et al., 2007)) .

1149 In figure 810, there are a few data points which are complete outliers. These correspond to
1150 simulations in the Ordovician; the outliers happen irrespective of the CO₂ model that is used.
1151 Inspection of these simulations shows that the cause for this discrepancy is related to two factors:
1152 1) a continental configuration with almost no land in the Northern hemisphere and , 2) a
1153 reconstruction which includes significant southern hemisphere ice cover (see fig.1 and fig 2).
1154 Combined, these factors produced a temperature structure which is highly non-symmetric, with the
1155 Southern high latitudes being more than 20°C colder than the Northern high latitudes. This anomaly
1156 biases the average polar temperatures shown in figure 810.

1157 3.5 Deep Ocean Temperature versus Global Mean Temperature

1158

1159 The relationships described above help to understand the overall relationship between deep ocean
1160 temperatures and global mean temperature. Figure 911 shows the correlation between modelled
1161 deep ocean temperatures (> 1000 m) and global mean surface air temperature, and figure 1012
1162 shows a comparison of changes in modelled deep ocean temperature compared to model global
1163 mean temperature throughout the Phanerozoic.

1164 The overall slope is 0.64 (0.59 to 0.69) with an $r^2 = 0.74$. If we consider the last 115 Ma (for which
1165 exists compiled benthic temperatures), then the slope is slightly steeper (0.67 with an $r^2 = 0.90$).
1166 Similarly, the “smooth”-CO₂ and the Foster-CO₂ simulation results have very different slopes. The
1167 “smooth”-CO₂ simulations have a slope of 0.47, whereas the Foster-CO₂ simulations have a slope of
1168 0.76. The root mean square departure from the regression line in figure 9 is 1.3°C 11 is 1.3°C.
1169 Although we could have used a non-linear fit as we might expect such a relationship if the pole-to-
1170 equator temperature gradient changes, all use of benthic temperatures as a global mean surface
1171 temperature proxy are based on linear relationship.

1172
1173 The relatively good correlations in the fig.911 are confirmed when examining fig.10a12a and
1174 10b12b. On average, the deep ocean temperatures tend to underestimate the global mean change
1175 (fig.10b12b) which is consistent with the regression slope being less than 1. However, the errors are

Formatt
Formatt
single, Sn

1209 substantial with largest errors occurring during the pre-Cretaceous and can be 4-6 °C. This is an
1210 appreciable error that would have a substantial impact on estimates of climate sensitivity. Even
1211 within the late Cretaceous and Cenozoic, the errors can exceed 2°C which can exceed 40% of the
1212 total change.

1213 The characteristics of the plots can best be understood in terms of figures (6 and 810). For instance,
1214 most of the Carboniferous simulations plot below the regression line because the polar SSTs are not
1215 well-correlated with the global mean temperature (figure 810). By contrast, the Triassic and Jurassic
1216 Foster CO₂ simulations plot above the regression line because the deep ocean temperature is not
1217 well-correlated with the polar temperatures (figure 6).

1218 4. Discussion and Conclusion

1219 The paper has presented the results from two unique sets of paleoclimate simulations covering the
1220 Phanerozoic. The focus of the paper has been to use the HadCM3L climate model to evaluate how
1221 well we can predict global mean surface temperatures from benthic foram data. This is an important
1222 consideration because benthic microfossil data are one of the few datasets used to directly estimate
1223 past global mean temperatures. Other methods, such as using planktonic foraminiferal estimates,
1224 are more challenging because the sample sites are geographically sparse, so it is difficult to
1225 accurately estimate the global mean temperature from highly variable and widely dispersed data.
1226 This is particularly an issue for older time periods when fewer isotopic measurements from
1227 planktonic microfossils are available, and can result in a bias because most of the isotopic
1228 temperature sample localities are from tropical latitudes (30°S – 30°N) (Song et al., 2019).

1229 By contrast, deep ocean temperatures are more spatially uniform. Hence, benthic foram data has
1230 frequently been used to estimate past global mean temperatures and climate sensitivity (Hansen et
1231 al., 2013). Estimates of uncertainty for deep ocean temperatures incorporate uncertainties from CO₂
1232 and from the conversion of δ¹⁸O measurements to temperature but have not been able to assess
1233 assumptions about the source regions for deep ocean waters and the importance polar
1234 amplification. Of course, in practice, lack of ocean sea floor means that benthic compilations exist
1235 only for the last 110Ma.

1236 Changes in heat transport also play a potentially important role in polar amplification. In the
1237 supplementary figure, we show the change in atmosphere and ocean poleward heat fluxes for each
1238 time period. Examination of the modelled poleward heat transport by the atmosphere and ocean
1239 shows a very complicated pattern, with all time periods showing the presence of some Bjerknes
1240 compensation (Bjerknes, 1964) (see (Outten et al., 2018) for example in CMIP5 models). Bjerknes
1241 compensation is where the change in ocean transport is largely balanced by an equal but opposite

1242 change in atmospheric transport. For instance, compared to present day, the mid-Cretaceous and
1243 Early Eocene warm simulations shows a large increase in northward atmospheric heat transport,
1244 linked with enhanced latent heat transport associated with the warmer, moister atmosphere.
1245 However, this is partly cancelled by an equal but opposite change in the ocean transport. E.g.
1246 compared to present day, the early Eocene northern hemisphere atmospheric heat transport
1247 increases by up to 0.5PW, but the ocean transport is reduced by an equal amount. The net
1248 transport from equator to the N.Pole changes by less than 0.1PW (i.e. less than 2% of total). Further
1249 back in time, the compensation is still apparent but the changes are more complicated, especially
1250 when the continents are largely in the Southern hemisphere. Understanding the causes of these
1251 transport changes will be the subject of another paper.

1252 We have shown that although the expected correlation between benthic temperatures and high-
1253 latitude surface temperatures exists, the correlation has considerable scatter. This is caused by
1254 several factors. Changing paleogeographies results in changing locations for deep water formation.
1255 Some paleogeographies result in significant deep-water formation in the Northern hemisphere (e.g.
1256 our present-day configuration) although for most of the Phanerozoic, the dominant source of deep-
1257 water formation has been southern hemisphere. Similarly, even when deep water is formed in just
1258 one hemisphere, there can be substantial regional and latitudinal variations in its location and the
1259 corresponding temperatures. Finally, during times of very warm climates (e.g. mid-Cretaceous) the
1260 overturning circulation can be very weak and there is a marked decoupling between the surface
1261 waters and deep ocean. In the HadCM3 model during hothouse time periods, high temperatures and
1262 high rates of evaporation produce hot and saline surface waters which sink to become intermediate
1263 and deep waters at low latitudes.

1264 Similar arguments can be made regarding the link between global mean temperature and the
1265 temperature at high latitudes. Particularly important is the area of land at the poles and the extent
1266 of sea ice/land ice. Colder climates and paleogeographic configurations with more land at the pole
1267 will result in a steeper latitudinal temperature gradient and hence exhibit a changing relationship
1268 between polar and global temperatures. But the fraction of land versus ocean is also important.

1269 Finally, the overall relationship between deep ocean temperatures and global mean temperature is
1270 shown to be relatively linear, but the slope is quite variable. In the model simulations using the
1271 “smooth” CO₂ curve, the slope is substantially shallower (0.48) than slope obtained using the Foster
1272 CO₂ curve (0.76). This is related to the different controls that CO₂ and paleogeography exert (as
1273 discussed above). In the simulation that uses the “smooth” CO₂ data set, the levels of CO₂ do not
1274 vary much, so the paleogeographic controls are more pronounced.

1275 This raises the interesting conundrum that when trying to use reconstructed deep ocean
1276 temperatures and CO₂ to estimate climate sensitivity, the interpreted global mean temperature also
1277 depends, in part, on the CO₂ concentrations. However, if we simply use the combined slope, then
1278 the root mean square error is approximately 1.4°C, and the maximum error is over 4°C. The root
1279 mean square error is a relatively small compared to the overall changes and hence the resulting
1280 uncertainty in climate sensitivity associated with this error is relatively small (~15%) and the CO₂
1281 uncertainty dominates. However, the maximum error is potentially more significant.

1282 Our work has not addressed other sources of uncertainty. In particular, it would be valuable to use a
1283 water isotope-enabled climate model to better address the uncertainties associated with the
1284 conversion of the observed benthic δ¹⁸O to temperature. This requires assumptions about the δ¹⁸O
1285 of sea water. We hope to perform such simulation in future work, though this is a particularly
1286 challenging computational problem because the isotope enabled model is significantly slower and
1287 the completion of the multi-millennial simulations required for deep ocean estimates would take
1288 more than 18 months to complete.

1289 Our simulations extend and develop those published by (Lunt et al., 2016), and (Farnsworth et al.,
1290 2019a; Farnsworth et al., 2019b). The simulations reported in this paper used the same climate
1291 model (HadCM3L) but used an improved ozone concentration and corrected a salinity drift that can
1292 lead to substantial changes over the duration of the simulation. Our simulations also use an
1293 alternative set of geographic reconstructions that cover a larger time period (540 Ma – Modern).
1294 They also include realistic land ice cover estimates, which were not included in the original
1295 simulations (except for the late Cenozoic) but generally have a small impact in the Mesozoic.

1296 Similarly, the new simulations use two alternative models for past atmospheric CO₂ use more
1297 realistic variations in CO₂ through time, (compared with idealised constant values in Farnsworth et al
1298 and Lunt et al), while at the same time recognizing the levels of uncertainty. Although the Foster CO₂
1299 curve is more directly constrained by CO₂ data, it should be noted that this data come from multiple
1300 proxies and there are large gaps in the data set. There is evidence that the different proxies have
1301 different biases and it is not obvious that the correct approach is to simply fit a Loess-type curve to
1302 the CO₂ data. This is exemplified by the Maastrichtian. The Foster Loess curve shows a minimum in
1303 CO₂ during the Maastrichtian which results in the modelled deep ocean temperatures being much
1304 too cold. However, detailed examination of the CO₂ data shows most of the Maastrichtian data is
1305 based on stomatal index reconstructions which often are lower than other proxies. Thus, the
1306 Maastrichtian low CO₂, relative to other periods, is potentially driven by changing the proxy rather
1307 than by real temporal changes.

1340 Though the alternative, “smooth” CO₂ curve is not the optimum fit to the data, it does pass through
1341 the cloud of individual CO₂ reconstructions and hence represents one possible “reality”. For the Late
1342 Cretaceous and Cenozoic, the “smooth” CO₂ simulation set does a significantly better job simulating
1343 the deep ocean temperatures of the Friedrich/Cramer/Zachos curve.

1344 Although the focus of the paper has been the evaluation of the modelled relationship between
1345 benthic and surface temperatures, the simulations are a potentially valuable resource for future
1346 studies. This includes using the simulations for paleoclimate/climate dynamic studies and for climate
1347 impact studies, such as ecological niche modelling. We have therefore made available on our
1348 website the results from our simulations

1349 (https://www.paleo.bristol.ac.uk/ummodel/scripts/papers/Valdes_et_al_2021.html)

1350 Data Availability

1351 All simulation data is available from:

1352 https://www.paleo.bristol.ac.uk/ummodel/scripts/papers/Valdes_et_al_2021.html

1353 Author contributions

1354 Study was developed by all authors. All model simulations were performed by PJV who also
1355 prepared the manuscript with contributions from all co-authors.

1356 Competing interests

1357 The authors declare that they have no conflict of interest

1358

1359

1360 Acknowledgments.

1361 DJL and PJV acknowledge funding from NERC through NE/P013805/1. The production of
1362 paleogeographic digital elevation models was funded by the sponsors of the PALEOMAP Project.
1363 This work is part of the PhanTASTIC project led by Scott Wing and Brian Huber from the Smithsonian
1364 Institution’s National Museum of Natural History and was initiated at a workshop supported by
1365 Roland and Debra Sauermann. This work was carried out using the computational facilities of the
1366 Advanced Computing Research Centre, University of Bristol (<http://www.bris.ac.uk/acrc/>). The
1367 authors declare that they have no competing interests. Data and materials availability: All data
1368 needed to evaluate the conclusions in the paper are present in the paper. Model data can be
1369 accessed at www.bridge.bris.ac.uk/resources/simulations.

1370

1371

Formatte

Formatte

Formatte

Formatte

Formatte

Formatte

Formatte

Formatte

Formatte

Formatte

Formatte

Formatte

1372

1373

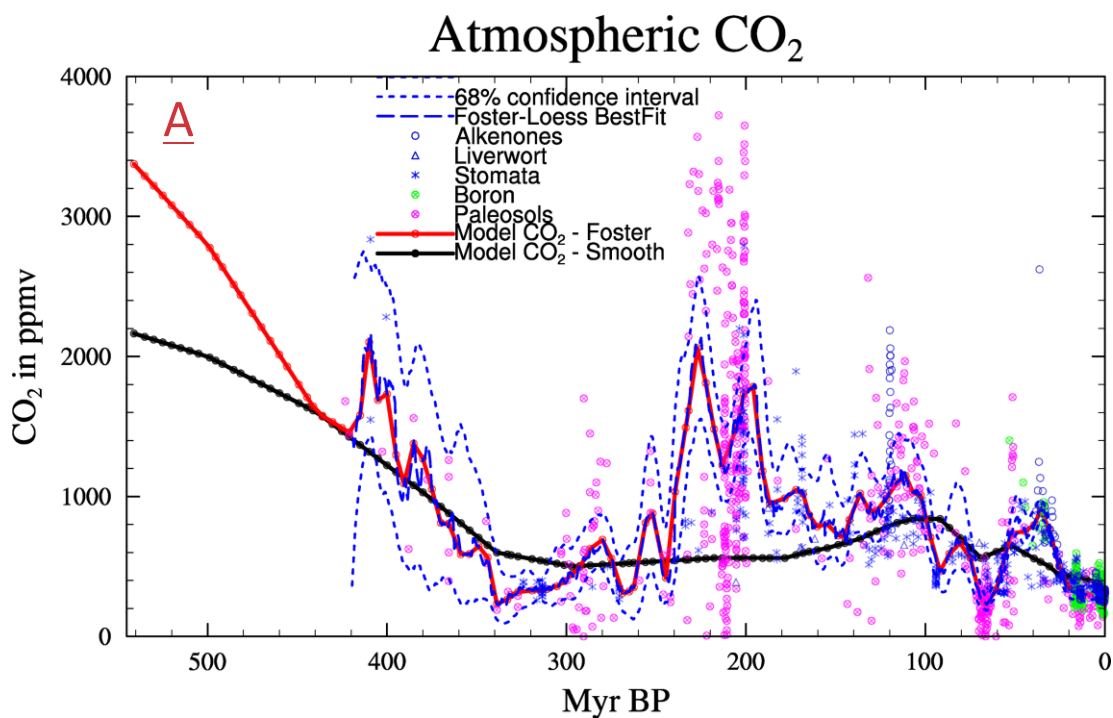
1374

1375

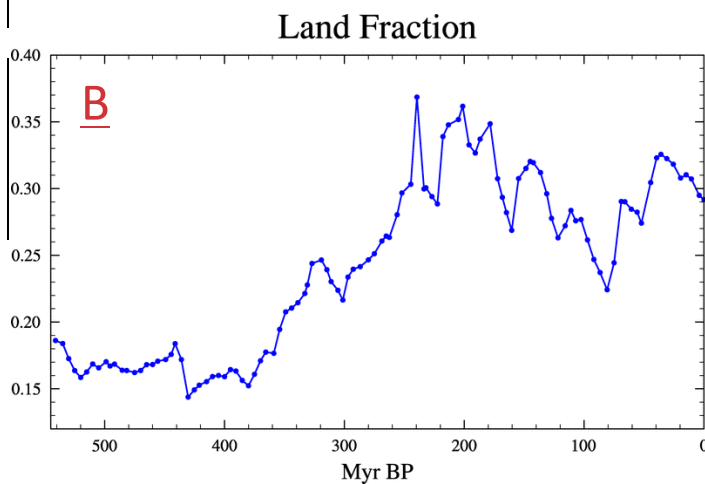
1388 Figures

1389 **Figure 1.** Summary of boundary condition changes to model of the Phanerozoic, (a) CO₂
1390 reconstructions (from Foster et al. 2017) and the two scenarios used in the models, (b) Land-sea
1391 fraction from the paleogeographic reconstructions, and (c) land ice area input into model. The
1392 paleogeographic reconstructions can be accessed at <https://www.earthbyte.org/paleodem->
1393 [resource-scotese-and-wright-2018/](https://www.earthbyte.org/paleodem-resource-scotese-and-wright-2018/). An animation of the high-resolution (1° x 1°) and model
1394 resolution (3.75° longitude x 2.5° latitude) maps can be found here:

1395 [https://www.paleo.bristol.ac.uk/~ggpjv/scotese/scotese_raw_moll.normal_scotese_moll.normal.ht](https://www.paleo.bristol.ac.uk/~ggpjv/scotese/scotese_raw_moll.normal_scotese_moll.normal.htm)
1396 [ml](https://www.paleo.bristol.ac.uk/~ggpjv/scotese/scotese_raw_moll.normal_scotese_moll.normal.htm)

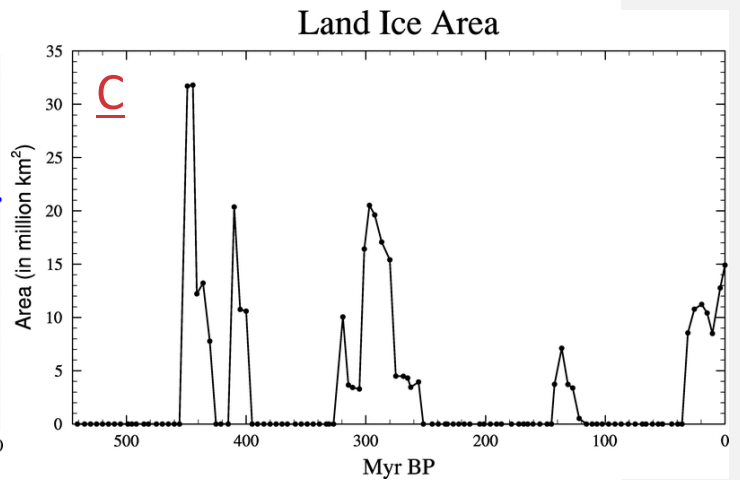


1397



1398

1399

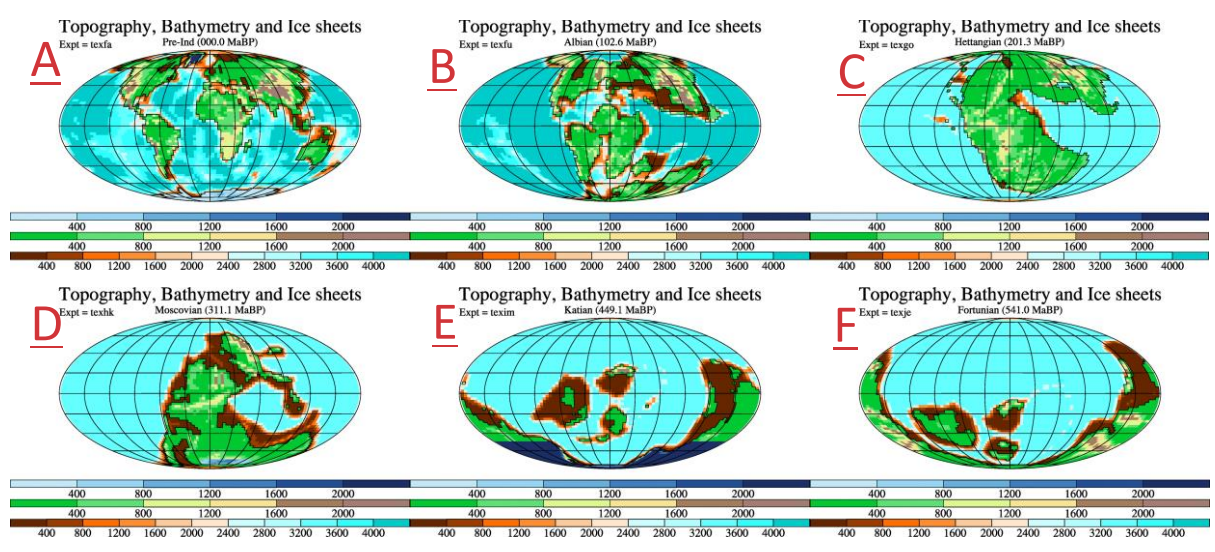


1419 **Figure 2.** A few example paleogeographies, once they have been re-gridded onto the HadCM3L grid.
1420 The examples are for (a) present day, (b) Albian, 102.6Ma (Lower Cretaceous), (c) Hettangian,
1421 201.3Ma (lower Jurassic), (d) Moscovian, 311.1Ma (Pennsylvanian, Carboniferous), (e) Katian,
1422 449.1Ma (Upper Ordovician), and (f) Fortunian, 541.0Ma (Cambrian). The top color legend refers to
1423 the height of the ice sheets (if they exist), the middle color legend refers to heights on land (except
1424 ice), and the lower color legend refers to the ocean bathymetry. All units are meters.

1425
1426

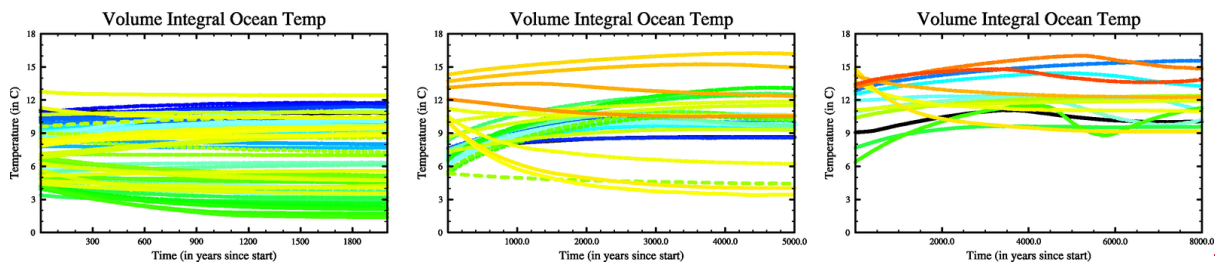
1427

1428
1429
1430
1431
1432
1433
1434
1435
1436
1437



1452 **Figure 3.** Time series of the annual, volume mean ocean temperature for all 109 simulations. (a)
1453 shows those simulations for which 2000 years was sufficient to satisfy the convergence criteria
1454 described in text (these were for all simulations listed in table 1 except those listed in (b) and (c)), (b)
1455 those simulation which required 5000 years (these were for all the simulations for 31.0, 35.9, 39.5,
1456 55.8, 60.6, 66.0, 69.0, 102.6, 107.0, 121.8, 127.2, 154.7, 160.4, 168.2, 172.2, 178.4, 186.8, 190.8,
1457 196.0, 201.3, 204.9, 213.2, 217.8, 222.4, 227.0, 232.0, and 233.6 Ma BP), and (c) those simulation
1458 which required 8000 years (these were simulations for 44.5, 52.2, 86.7, 91.9, 97.2, 111.0, 115.8,
1459 131.2, 136.4, 142.4, 145.0, 148.6, 164.8, and 239.5 Ma BP). The different coloured lines show the
1460 different runs. The plot simply show the extent to which all runs have reached steady state. For
1461 more details about specific simulations, please see the supplementary figures.

1462

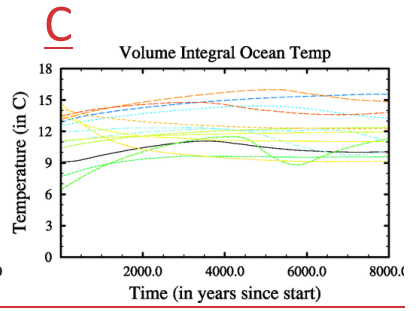
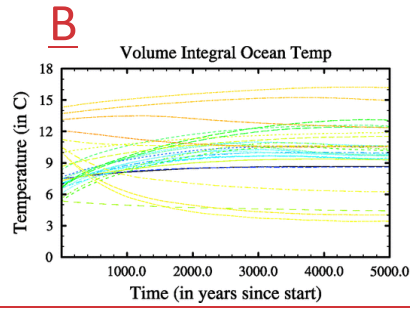
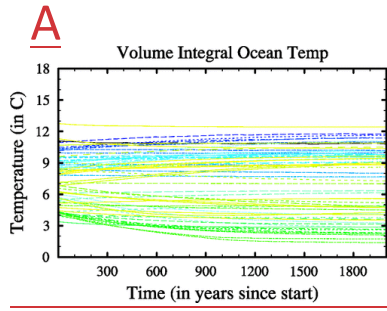


1463

1464

1465

1466

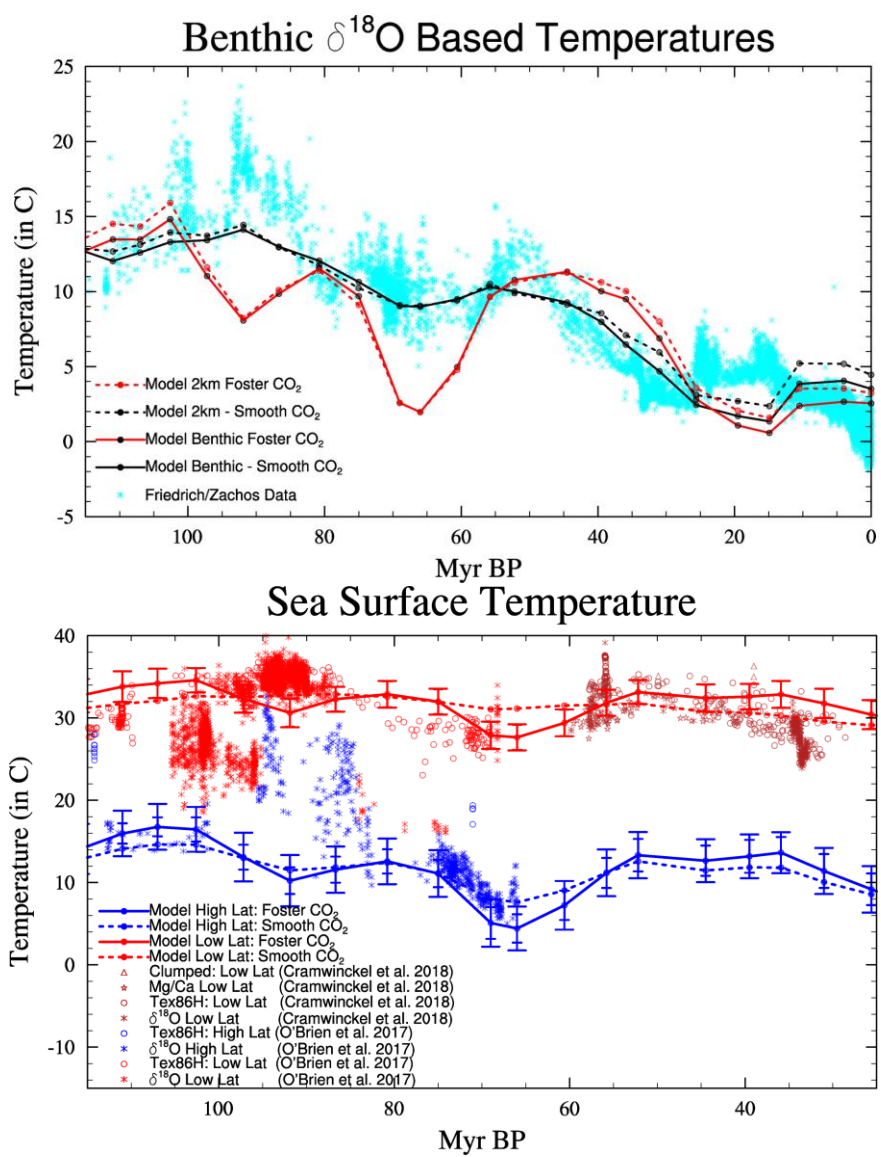


1467

1468

1469

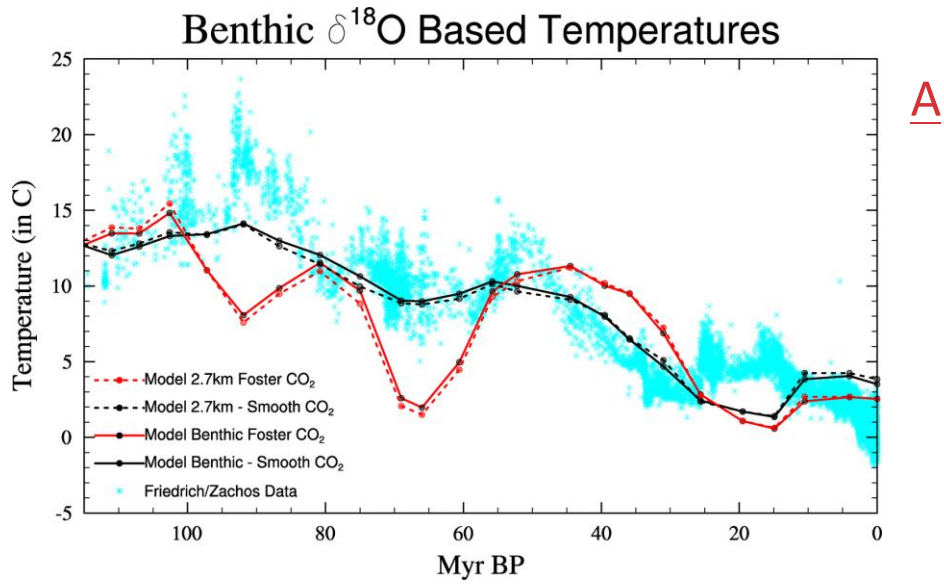
1482 **Figure 4.** (a) Comparison of modelled deep ocean temperatures versus those from (Zachos et al.,
 1483 2008)(Zachos et al., 2008) and (Friedrich et al., 2012)(Friedrich et al., 2012) converted to
 1484 temperature using the formulation in (Hansen et al., 2013). The model temperatures are global
 1485 averages over the bottom layer of the model but excludes shallow marine settings (less than
 1486 300m-1000m). The dashed lines show the modelled global average ocean temperatures at the model
 1487 layer centered at 2116m-2731m, and (b) Comparison of modelled sea surface temperatures with the
 1488 compilations of (O'Brien et al., 2017) and (Cramwinckel et al., 2018). The data is a combination of
 1489 Tex_{86} (using the TexH calibration), $\delta^{18}O$ (using Bemis et al. calibration, with a correction for the
 1490 latitudinal gradient of $\delta^{18}O$), Mg/Ca, and clumped Isotope data (from (Evans et al., 2018)). The
 1491 model data shows low latitude temperatures (averaged from 10S to 10N) and high latitude
 1492 temperatures (averaged over 47.5N to 65N and 47.5S to 65S). The Foster- CO_2 simulations also show
 1493 a measure of the spatial variability. The large bars show the spatial standard deviation across the



B

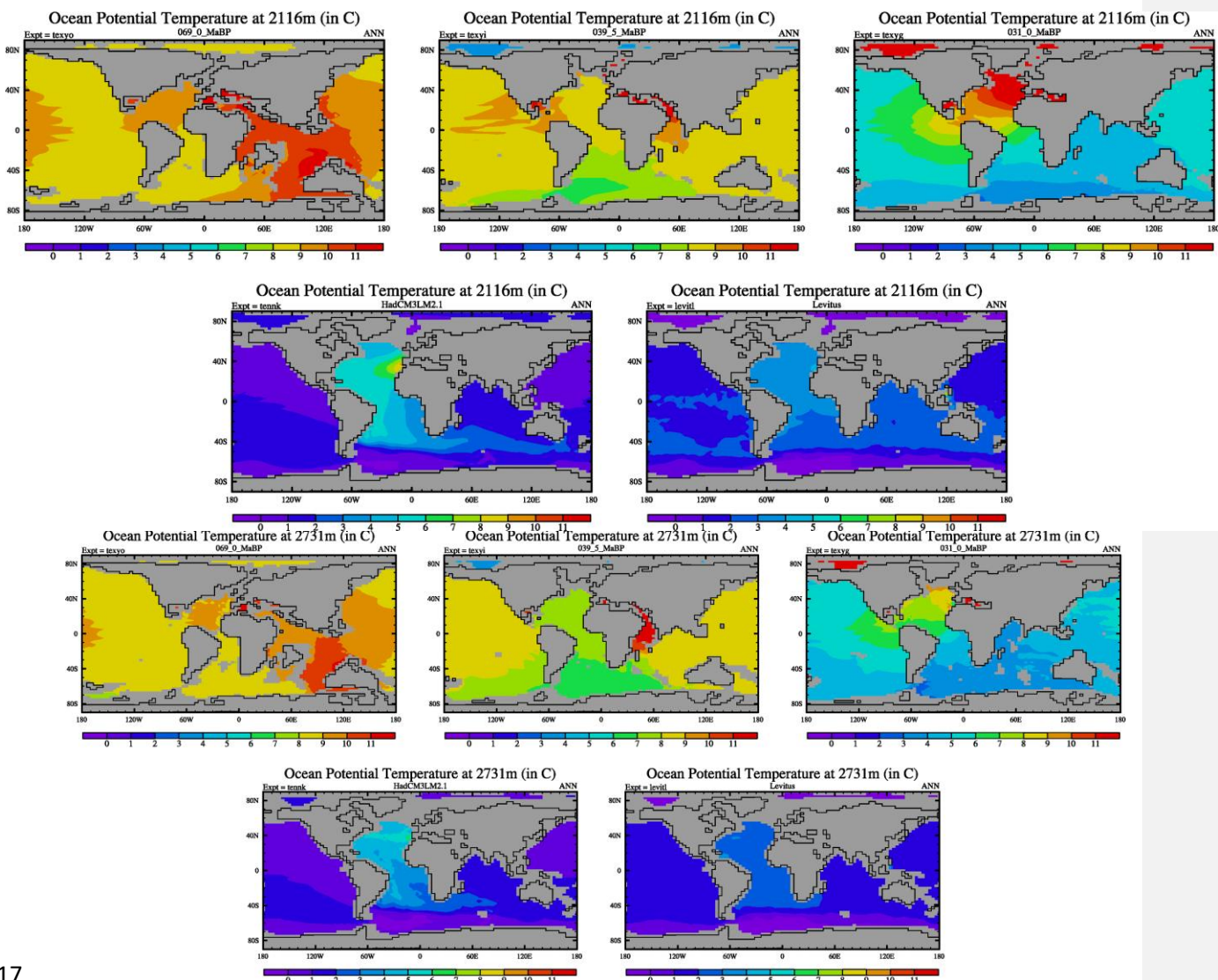
1494 whole region, and the smaller bars shows the average spatial standard deviation along longitudes
1495 within the region. Note that the ranges of both the x and y-axis differ between (a) and (b).

1496



1508 **Figure 5.** Modelled annual mean ocean temperatures are ~~2116m~~2731m depth for three example
1509 past time periods. The left figure is for the late Cretaceous, the center for the late Eocene (39.5Ma),
1510 and the right for the Oligocene (31Ma). These are results from the smooth-CO₂ set of simulations
1511 which agree better with the observed benthic temperature data. Also included are the pre-industrial
1512 simulation and World Ocean Atlas 1994 observational data, provided by the NOAA-ESRL Physical
1513 Sciences Laboratory, Boulder Colorado from their web site at <https://psl.noaa.gov/>. The thin black
1514 lines show the coastlines, and the grey areas are showing where the ocean is shallower than
1515 ~~2116m~~2731m.

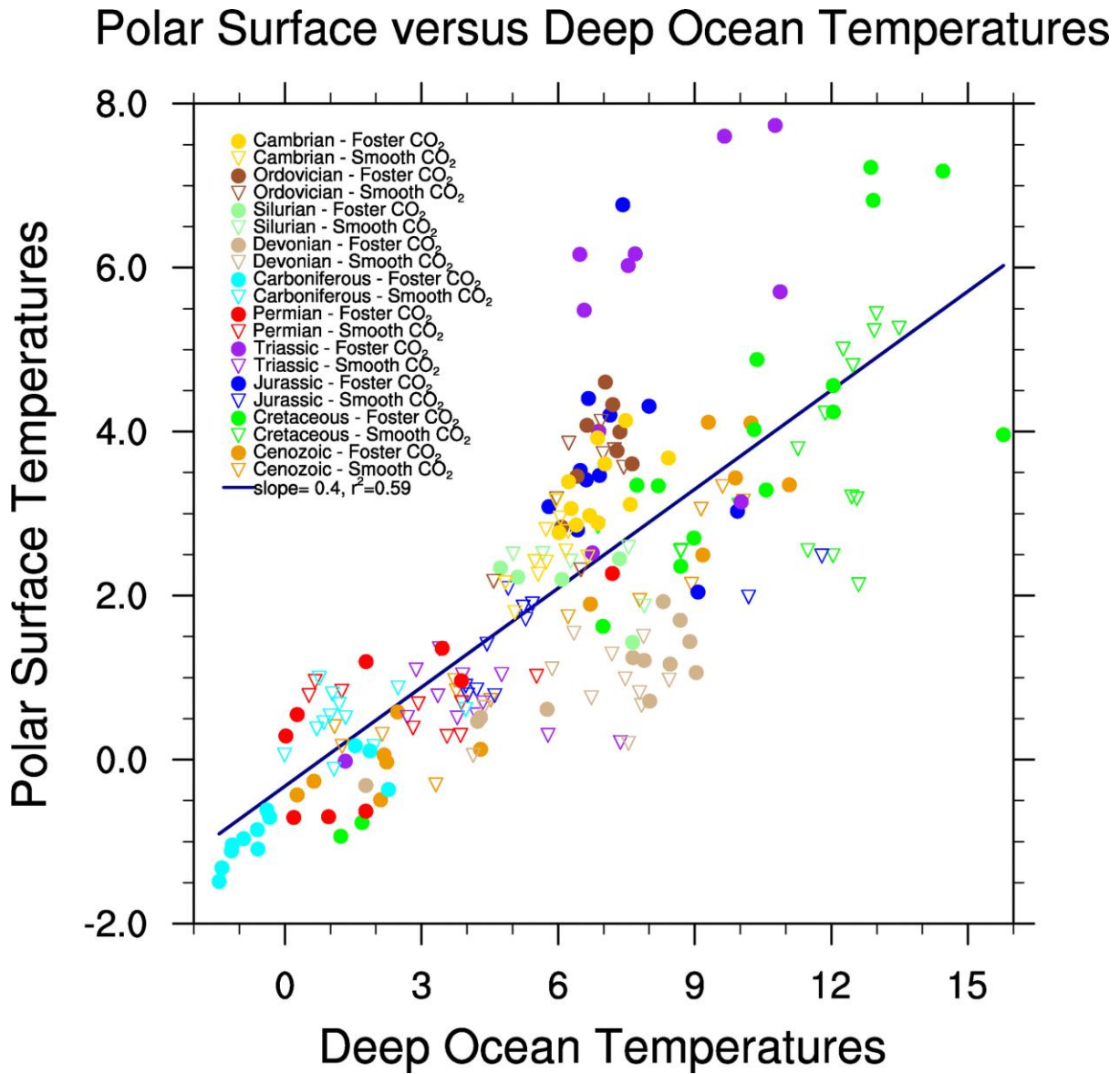
1516



1517

1518

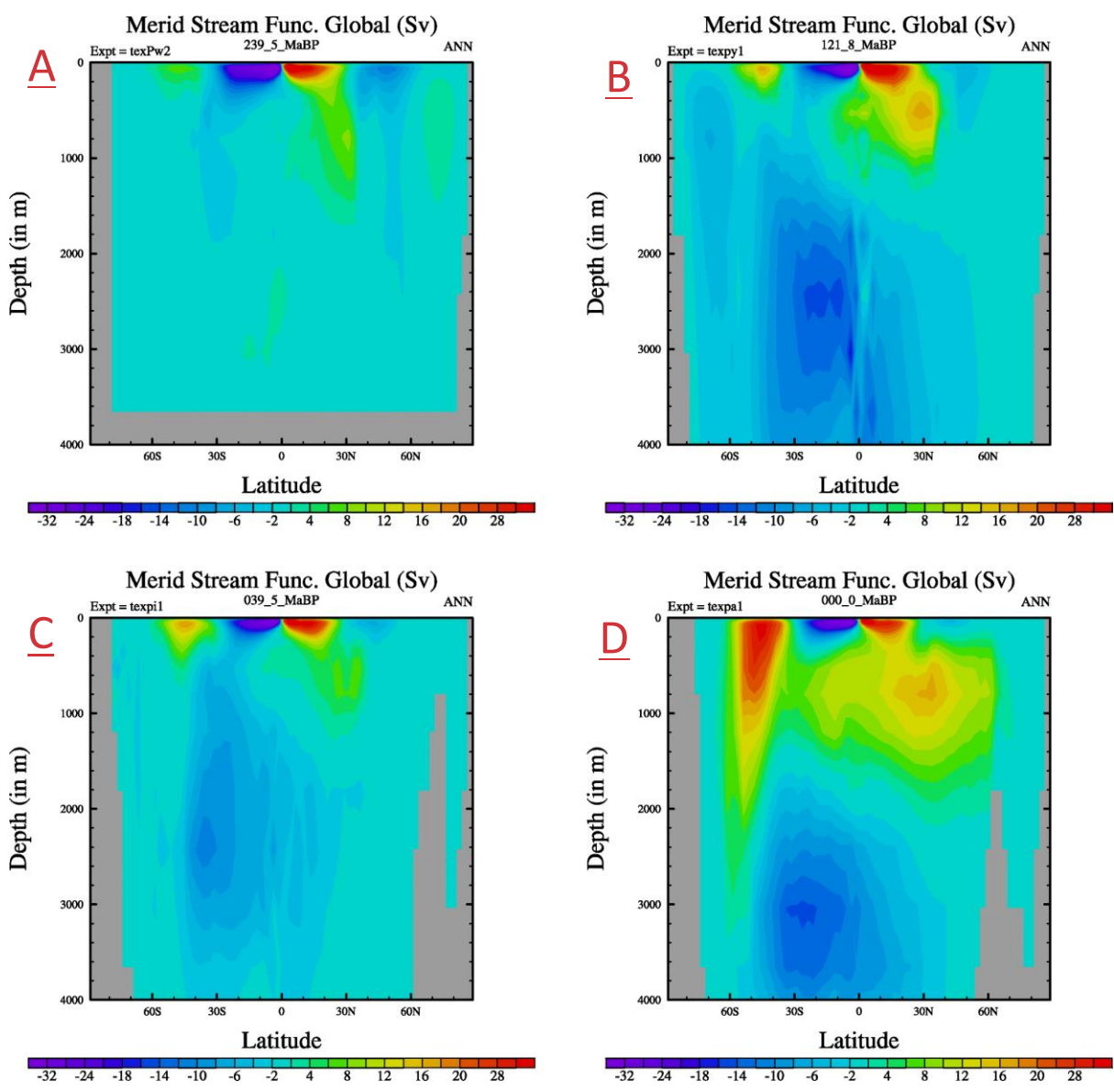
1519 **Figure 6.** Correlations between deep ocean temperatures and surface polar sea surface
1520 temperatures. The deep ocean temperatures are defined as the average temperature at the bottom
1521 of the model ocean, where the bottom must be deeper than 1000m. The polar sea surface
1522 temperatures are the average winter (i.e. northern polar in DJF and southern polar in JJA) sea
1523 surface temperature polewards of 60°. The inverted triangles show the results from the smooth CO₂
1524 simulations and the dots refer to the Foster CO₂ simulations. The colors refer to different geological
1525 era.



1526

1536 **Figure 7.** Global Ocean overturning circulation (in Sverdrup) for four different time periods for the
1537 Foster-CO₂ simulations. Positive (yellow/red) values correspond to a clockwise circulation, negative
1538 (dark blue/purple) values represent an anti-clockwise circulation. **Top-left:(a)** Middle Triassic,
1539 Ladinian, 239.5Ma, **top-right:(b)** Lower Cretaceous, Aptian, 121.8 Ma, **bottom-left:(c)** Late Eocene,
1540 Bartonian, 39.5Ma, and **bottom-right:(d)** Present Day. Paleogeographic reconstructions older than
1541 the oldest ocean floor (~Late-Jurassic) have uniform deep ocean floor depth.

1542



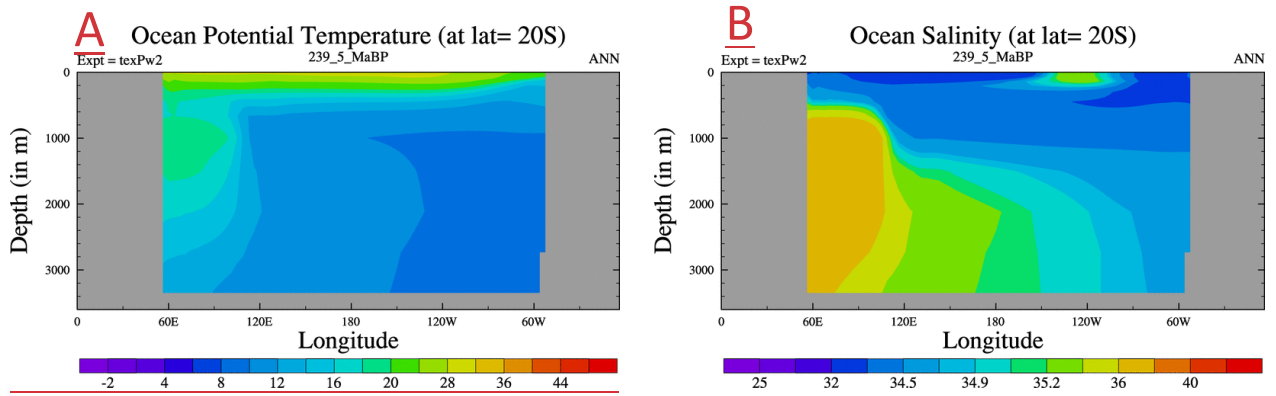
1543

1544

1545 **Figure 8.**

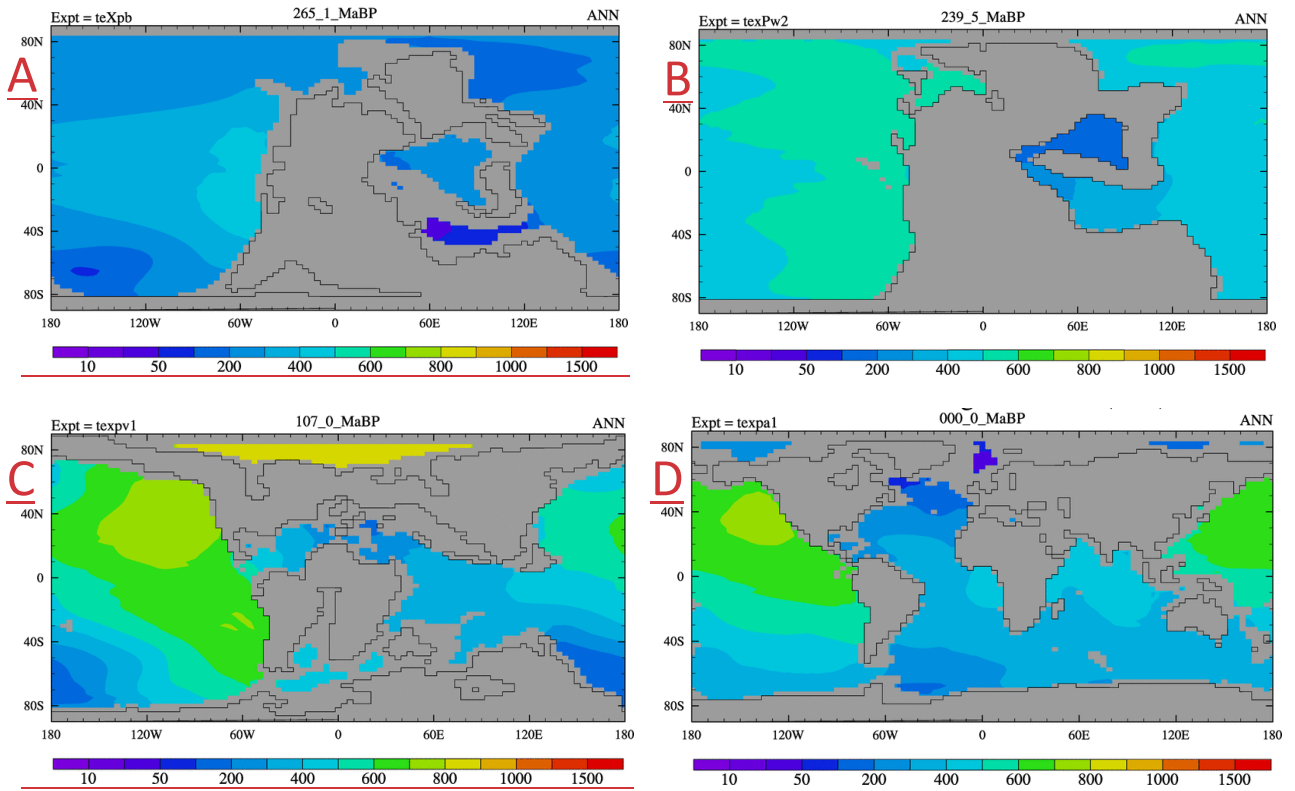
1546
1547
1548
1549

Figure 8. Longitudinal cross section at 20S of (a) ocean potential temperature and (b) salinity for the Ladanian (240Ma). Temperature is in C and salinity is in PSU.



1550
1551
1552

1553 **Figure 9.** Modelled age of water tracer at 2731m for 4 different time periods (a) 265Ma, (b) 240Ma,
1554 (c) 107Ma, and (d) 0Ma. Units are years.

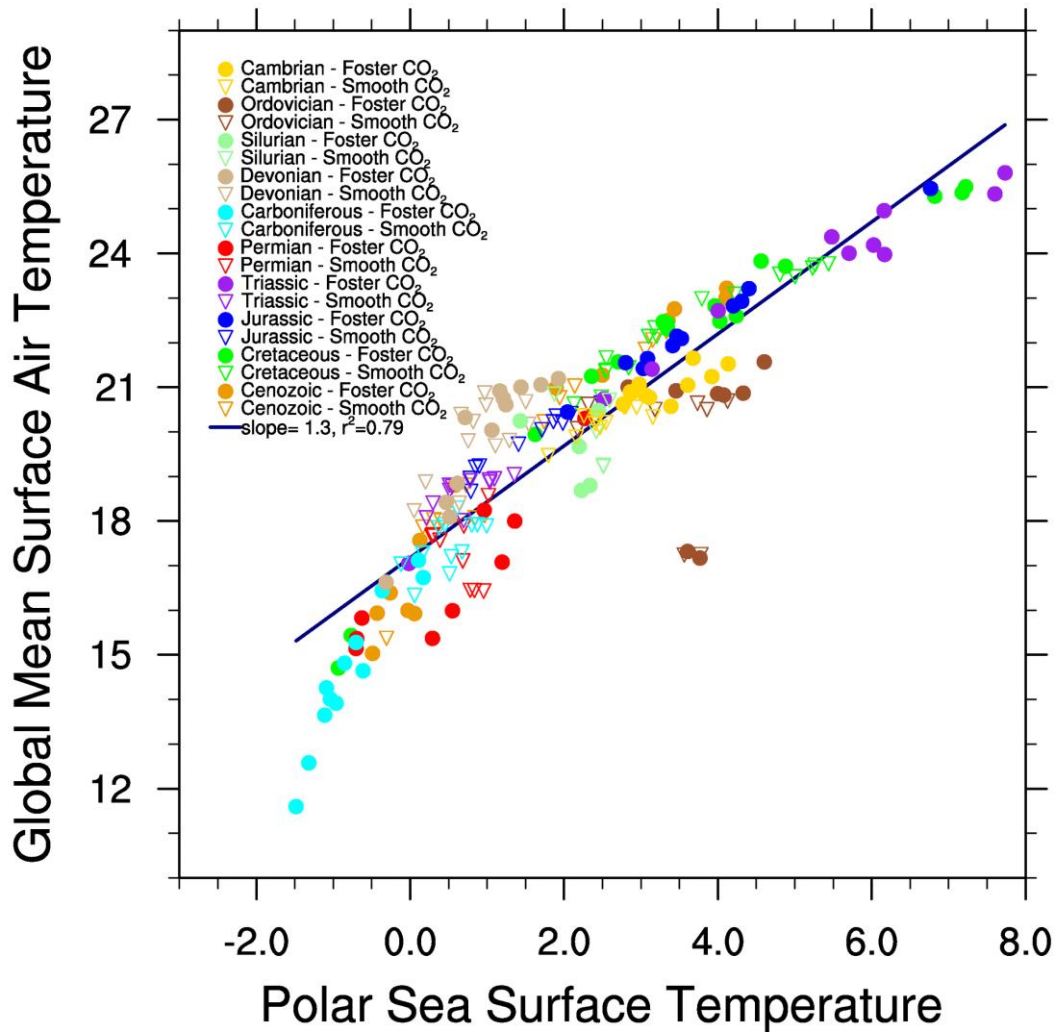


1562 **Figure 10.** Correlation between high latitude ocean temperatures (polewards of 60°) and the annual
1563 mean, global mean surface air temperature. The polar temperatures are the average of the two
1564 winter hemispheres (i.e. northern DJF and southern JJA). Other details as in figure 6.

1565

1566

Global Mean Surface Air Temperature versus Polar SST



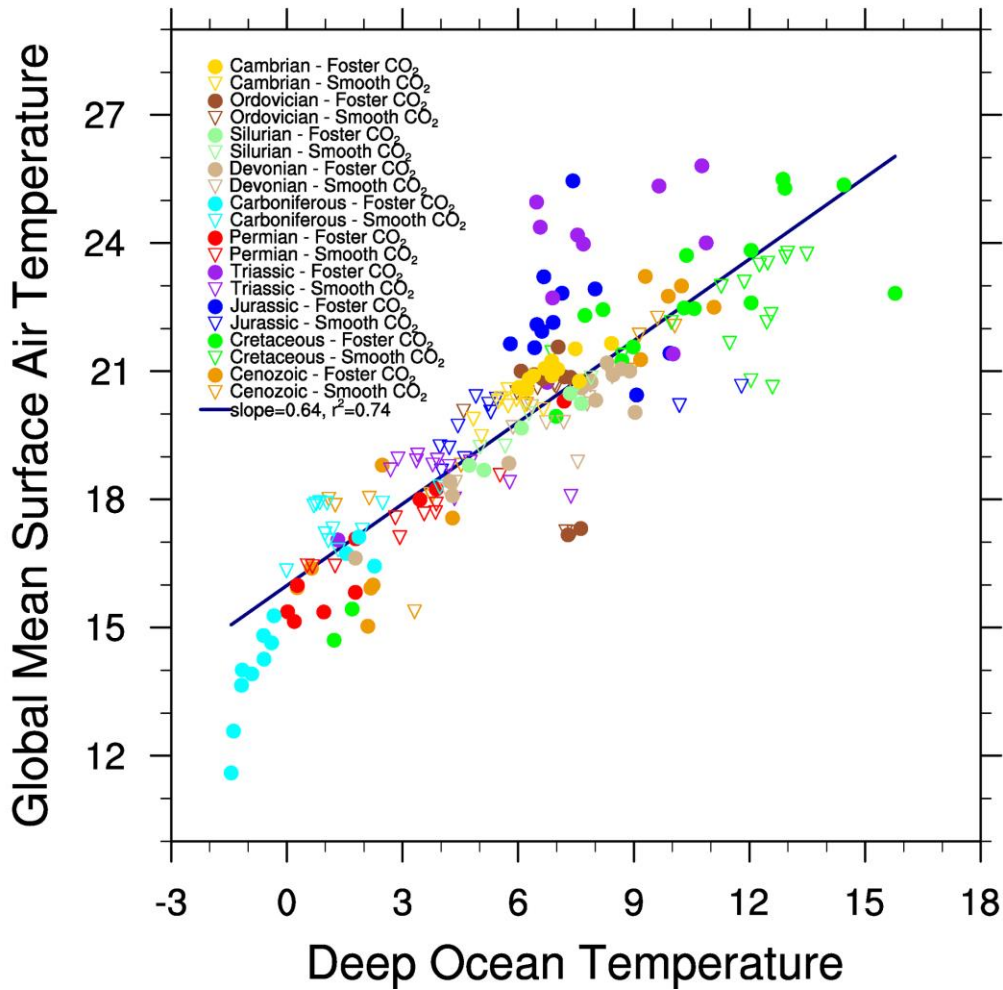
1567

1575 **Figure 911.** Correlation between the global mean, annual mean surface air temperature and the
1576 deep ocean temperature. The deep ocean temperatures are defined as the average temperature at
1577 the bottom of the model ocean, where the bottom must be deeper than 1000m. Other details as in
1578 figure 6.

Formatt
Formatt

1579

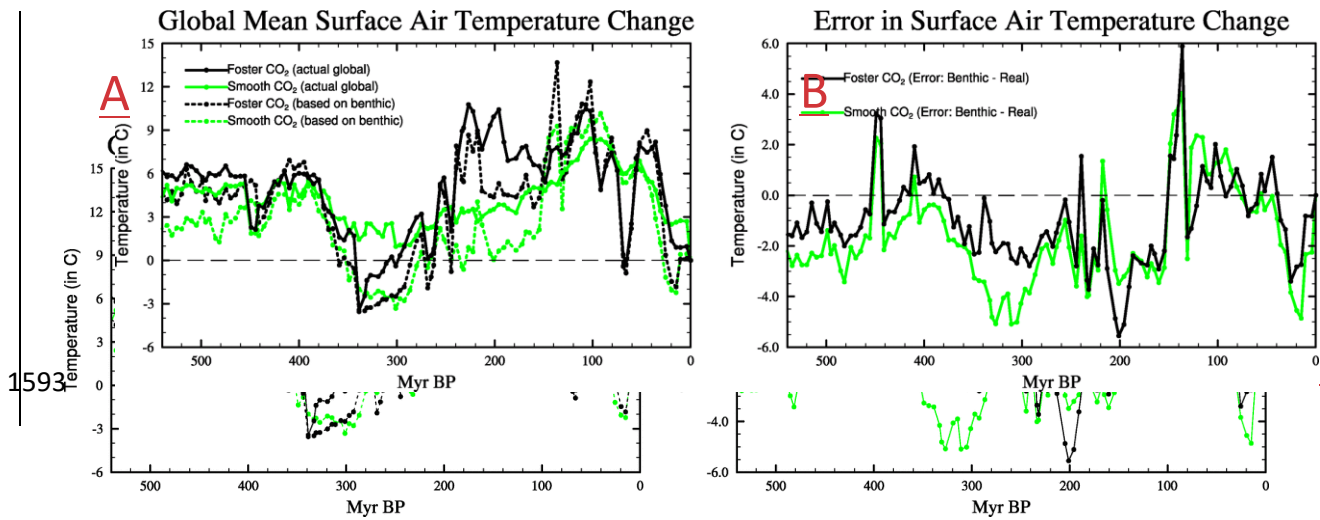
Surface Air Temperature versus Deep Ocean Temperature



1580

1581

1588 **Figure 1012.** Phanerozoic Time series of modelled temperature change (relative to pre-Industrial) for
 1589 the smooth (green lines) and Foster-CO₂ (black) simulations (a) shows the actual modelled global
 1590 mean surface air temperature (solid lines) whereas the dashed line shows the estimate based on
 1591 deep ocean temperatures, and (b) error in the estimate of global mean temperature change if based
 1592 on deep ocean temperatures (i.e. deep ocean – global mean surface temperatures).



1644 References

- 1645 Alexeev, V.A., Langen, P.L., Bates, J.R., 2005. Polar amplification of surface warming on an
1646 aquaplanet in "ghost forcing" experiments without sea ice feedbacks. *Clim. Dyn.* 24, 655-666.
- 1647 Baatsen, M., van Hinsbergen, D.J.J., von der Heydt, A.S., Dijkstra, H.A., Sluijs, A., Abels, H.A., Bijl, P.K.,
1648 2016. Reconstructing geographical boundary conditions for palaeoclimate modelling during the
1649 Cenozoic. *Clim. Past.* 12, 1635-1644.
- 1650 [Baatsen, M.L.J., von der Heydt, A.S., Kliphuis, M., Viebahn, J., Dijkstra, H.A., 2018. Multiple states in](#)
1651 [the late Eocene ocean circulation. *Glob. Planet. Change* 163, 18-28.](#)
- 1652 [Barron, E.J., Peterson, W.H., 1990. MID-CRETACEOUS OCEAN CIRCULATION: RESULTS FROM MODEL](#)
1653 [SENSITIVITY STUDIES. *Paleoceanography* 5, 319-337.](#)
- 1654 Beerling, D.J., Fox, A., Stevenson, D.S., Valdes, P.J., 2011. Enhanced chemistry-climate feedbacks in
1655 past greenhouse worlds. *P Natl Acad Sci USA* 108, 9770-9775.
- 1656 [Bjerknes, J., 1964. Atlantic Air-Sea Interaction, in: Landsberg, H.E., Van Mieghem, J. \(Eds.\), 0065-](#)
1657 [2687. Elsevier, pp. 1-82.](#)
- 1658 Brass, G.W., Southam, J.R., Peterson, W.H., 1982. Warm Saline Bottom Water in the Ancient Ocean.
1659 *Nature* 296, 620-623.
- 1660 Cramer, B.S., Toggweiler, J.R., Wright, J.D., Katz, M.E., Miller, K.G., 2009. Ocean overturning since the
1661 Late Cretaceous: Inferences from a new benthic foraminiferal isotope compilation.
1662 *Paleoceanography* 24.
- 1663 Cramwinckel, M.J., Huber, M., Kocken, I.J., Agnini, C., Bijl, P.K., Bohaty, S.M., Frieling, J., Goldner, A.,
1664 Hilgen, F.J., Kip, E.L., Peterse, F., van der Ploeg, R., Rohl, U., Schouten, S., Sluijs, A., 2018.
1665 Synchronous tropical and polar temperature evolution in the Eocene. *Nature* 559, 382-+.
- 1666 Dietmuller, S., Ponater, M., Sausen, R., 2014. Interactive ozone induces a negative feedback in CO₂-
1667 driven climate change simulations. *J. Geophys. Res.-Atmos.* 119, 1796-1805.
- 1668 [Evans, D., Sagoo, N., Renema, W., Cotton, L.J., Muller, W., Todd, J.A., Saraswati, P.K., Stassen, P.,](#)
1669 [Ziegler, M., Pearson, P.N., Valdes, P.J., Affek, H.P., 2018. Eocene greenhouse climate revealed by](#)
1670 [coupled-clumped isotope-Mg/Ca thermometry. *P Natl Acad Sci USA* 115, 1174-1179.](#)
- 1671 [Donnadieu, Y., Puceat, E., Moiroud, M., Guillocheau, F., Deconinck, J.F., 2016. A better-ventilated](#)
1672 [ocean triggered by Late Cretaceous changes in continental configuration. *Nat Commun* 7, 12.](#)
- 1673 [Emiliani, C., 1954. Temperatures of Pacific Bottom Waters and Polar Superficial Waters during the](#)
1674 [Tertiary. *Science* 119, 853-855.](#)
- 1675 [England, M.H., 1995. The Age Of Water And Ventilation Timescales In A Global Ocean Model. *J Phys*](#)
1676 [Oceanogr](#) 25, 2756-2777.
- 1677 Farnsworth, A., Lunt, D.J., O'Brien, C.L., Foster, G.L., Inglis, G.N., Markwick, P., Pancost, R.D.,
1678 Robinson, S.A., 2019a. Climate Sensitivity on Geological Timescales Controlled by Nonlinear
1679 Feedbacks and Ocean Circulation. *Geophys. Res. Lett.* 46, 9880-9889.
- 1680 Farnsworth, A., Lunt, D.J., Robinson, S.A., **Valdes, P.J.**, Roberts, W.H.G., Clift, P.D., Markwick, P., Su,
1681 T., Wrobel, N., Bragg, F., Kelland, S.J., Pancost, R.D., 2019b. Past East Asian monsoon evolution
1682 controlled by paleogeography, not CO₂. *Sci Adv* 5.
- 1683 Foster, G.L., Royer, D.L., Lunt, D.J., 2017. Future climate forcing potentially without precedent in the
1684 last 420 million years. *Nat Commun* 8.
- 1685 Friedrich, O., Norris, R.D., Erbacher, J., [2011. Evolution of Cretaceous oceans: A 55 million year](#)
1686 [record of Earth's temperature and carbon cycle. *Grzyb Found Spec Pub* 17, 85-85.](#)
- 1687 [Friedrich, O., Norris, R.D., Erbacher, J., 2012. Evolution of middle to Late Cretaceous oceans-A 55](#)
1688 [m.y. record of Earth's temperature and carbon cycle. *Geology* 40, 107-110.](#)
- 1689 [Goldner, A., Herold, N., Huber, M., 2014. The challenge of simulating the warmth of the mid-](#)
1690 [Miocene climatic optimum in CESM1. *Clim. Past.* 10, 523-536.](#)
- 1691 Gordon, C., Cooper, C., Senior, C.A., Banks, H., Gregory, J.M., Johns, T.C., Mitchell, J.F.B., Wood, R.A.,
1692 2000. The simulation of SST, sea ice extents and ocean heat transports in a version of the Hadley
1693 Centre coupled model without flux adjustments. *Clim. Dyn.* 16, 147-168.

1694 Gough, D.O., 1981. Solar Interior Structure and Luminosity Variations. *Sol Phys* 74, 21-34.

1695 Gregory, J.M., Ingram, W.J., Palmer, M.A., Jones, G.S., Stott, P.A., Thorpe, R.B., Lowe, J.A., Johns,

1696 T.C., Williams, K.D., 2004. A new method for diagnosing radiative forcing and climate sensitivity.

1697 *Geophys. Res. Lett.* 31.

1698 Hansen, J., Sato, M., Kharecha, P., Beerling, D., Berner, R., Masson-Delmotte, V., Pagani, M., Raymo,

1699 M., Royer, D.L., Zachos, J.C., 2008. Target atmospheric CO₂: Where should humanity aim? *Open*

1700 *Atmos. Sci. J.* 2, 217-231.

1701 Hansen, J., Sato, M., Russell, G., Kharecha, P., 2013. Climate sensitivity, sea level and atmospheric

1702 carbon dioxide. *Philos T R Soc A* 371.

1703 Hansen, J.E., Sato, M., 2012. *Paleoclimate Implications for Human-Made Climate Change*. Springer

1704 Vienna, Vienna, pp. 21-47.

1705 [Hardiman, S.C., Andrews, M.B., Andrews, T., Bushell, A.C., Dunstone, N.J., Dyson, H., Jones, G.S.,](#)

1706 [Knight, J.R., Neininger, E., O'Connor, F.M., Ridley, J.K., Ringer, M.A., Scaife, A.A., Senior, C.A., Wood,](#)

1707 [R.A., 2019. The Impact of Prescribed Ozone in Climate Projections Run With HadGEM3-GC3.1. *J Adv*](#)

1708 [Model Earth Sy](#) 11, 3443-3453.

1709 Harris, J., Ashley, A., Otto, S., Valdes, P., Crossley, R., Preston, R., Watson, J., Goodrich, M., Team.,

1710 M.P., 2017. Paleogeography and Paleo-Earth Systems in the Modeling of Marine Paleoproductivity: A

1711 Prerequisite for the Prediction of Petroleum Source Rocks, in: Mahdi A. AbuAli, I.M., and Hege M.

1712 Nordgård Bolås (Ed.), *Petroleum Systems Analysis—Case Studies*. AAPG Memoir, pp. 27-60.

1713 Henkes, G.A., Passey, B.H., Grossman, E.L., Shenton, B.J., Yancey, T.E., Perez-Huerta, A., 2018.

1714 Temperature evolution and the oxygen isotope composition of Phanerozoic oceans from carbonate

1715 clumped isotope thermometry. *Earth Planet. Sci. Lett.* 490, 40-50.

1716 Holland, M.M., Bitz, C.M., 2003. Polar amplification of climate change in coupled models. *Clim. Dyn.*

1717 21, 221-232.

1718 [Kageyama, M., Albani, S., Braconnot, P., Harrison, S.P., Hopcroft, P.O., Ivanovic, R.F., Lambert, F.,](#)

1719 [Marti, O., Peltier, W.R., Peterschmitt, J.Y., Roche, D.M., Tarasov, L., Zhang, X., Brady, E.C., Haywood,](#)

1720 [A.M., LeGrande, A.N., Lunt, D.J., Mahowald, N.M., Mikolajewicz, U., Nisancioglu, K.H., Otto-Bliesner,](#)

1721 [B.L., Renssen, H., Tomas, R.A., Zhang, Q., Abe-Ouchi, A., Bartlein, P.J., Cao, J., Li, Q., Lohmann, G.,](#)

1722 [Ohgaito, R., Shi, X.X., Volodin, E., Yoshida, K., Zhang, X., Zheng, W.P., 2017. The PMIP4 contribution](#)

1723 [to CMIP6-Part 4: Scientific objectives and experimental design of the PMIP4-CMIP6 Last Glacial](#)

1724 [Maximum experiments and PMIP4 sensitivity experiments. *Geosci Model Dev* 10, 4035-4055.](#)

1725 Kennett, J.P., Stott, L.D., 1991. Abrupt Deep-Sea Warming, Palaeoceanographic Changes and Benthic

1726 Extinctions at the End of the Paleocene. *Nature* 353, 225-229.

1727 Kiehl, J.T., Shields, C.A., 2013. Sensitivity of the Palaeocene-Eocene Thermal Maximum climate to

1728 cloud properties. *Philos T R Soc A* 371.

1729 [Knorr, G., Butzin, M., Micheels, A., Lohmann, G., 2011. A warm Miocene climate at low atmospheric](#)

1730 [CO₂ levels. *Geophys. Res. Lett.* 38, 5.](#)

1731 [Krapp, M., Jungclaus, J.H., 2011. The Middle Miocene climate as modelled in an atmosphere-ocean-](#)

1732 [biosphere model. *Clim. Past.* 7, 1169-1188.](#)

1733 [Ladant, J.B., Poulsen, C.J., Fluteau, F., Tabor, C.R., MacLeod, K.G., Martin, E.E., Haynes, S.J., Rostami,](#)

1734 [M.A., 2020. Paleogeographic controls on the evolution of Late Cretaceous ocean circulation. *Clim.*](#)

1735 [Past.](#) 16, 973-1006.

1736 [Lunt, D.J., Bragg, F., Chan, W.L., Hutchinson, D.K., Ladant, J.B., Morozova, P., Niezgodzki, I., Steinig,](#)

1737 [S., Zhang, Z., Zhu, J., Abe-Ouchi, A., Anagnostou, E., de Boer, A.M., Coxall, H.K., Donnadieu, Y.,](#)

1738 [Foster, G., Inglis, G.N., Knorr, G., Langebroek, P.M., Lear, C.H., Lohmann, G., Poulsen, C.J., Sepulchre,](#)

1739 [P., Tierney, J.E., Valdes, P.J., Volodin, E.M., Dunkley Jones, T., Hollis, C.J., Huber, M., Otto-Bliesner,](#)

1740 [B.L., 2021. DeepMIP: model intercomparison of early Eocene climatic optimum \(EECO\) large-scale](#)

1741 [climate features and comparison with proxy data. *Clim. Past* 17, 203-227.](#)

1742 [Lunt, D.J., Dunkley Jones, T., Heinemann, M., Huber, M., LeGrande, A., Winguth, A., Loptson, C.,](#)

1743 [Marotzke, J., Roberts, C.D., Tindall, J., Valdes, P., Winguth, C., 2012. A model-data comparison for a](#)

1744 [multi-model ensemble of early Eocene atmosphere-ocean simulations: EoMIP. *Clim. Past.* 8, 1717-](#)
1745 [1736.](#)

1746 Lunt, D.J., Farnsworth, A., Loptson, C., Foster, G.L., Markwick, P., O'Brien, C.L., Pancost, R.D.,
1747 Robinson, S.A., Wrobel, N., 2016. Palaeogeographic controls on climate and proxy interpretation.
1748 *Clim. Past.* 12, 1181-1198.

1749 Lunt, D.J., [Huber, M., Anagnostou, E., Baatsen, M.L.J., Caballero, R., DeConto, R., Dijkstra, H.A.,](#)
1750 [Donnadieu, Y., Evans, D., Feng, R., Foster, G.L., Gasson, E., von der Heydt, A.S., Hollis, C.J., Inglis,](#)
1751 [G.N., Jones, S.M., Kiehl, J., Turner, S.K., Korty, R.L., Kozdon, R., Krishnan, S., Ladant, J.B., Langebroek,](#)
1752 [P., Lear, C.H., LeGrande, A.N., Littler, K., Markwick, P., Otto-Bliesner, B., Pearson, P., Poulsen, C.J.,](#)
1753 [Salzmann, U., Shields, C., Snell, K., Starz, M., Super, J., Tabor, C., Tierney, J.E., Tourte, G.J.L., Tripathi,](#)
1754 [A., Upchurch, G.R., Wade, B.S., Wing, S.L., Winguth, A.M.E., Wright, N.M., Zachos, J.C., Zeebe, R.E.,](#)
1755 [2017. The DeepMIP contribution to PMIP4: experimental design for model simulations of the EECO,](#)
1756 [PETM, and pre-PETM \(version 1.0\). *Geosci Model Dev* 10, 889-901.](#)

1757 [Lunt, D.J.,](#) Valdes, P.J., Dunkley Jones, T., Ridgwell, A., Haywood, A.M., Schmidt, D.N., Marsh, R.,
1758 Maslin, M., 2010. CO₂-driven ocean circulation changes as an amplifier of Paleocene-Eocene thermal
1759 maximum hydrate destabilization. *Geology* 38, 875-878.

1760 Murphy, D.P., Thomas, D.J., 2012. Cretaceous deep-water formation in the Indian sector of the
1761 Southern Ocean. *Paleoceanography* 27.

1762 Nowack, P.J., Abraham, N.L., Maycock, A.C., Braesicke, P., Gregory, J.M., Joshi, M.M., Osprey, A.,
1763 Pyle, J.A., 2015. A large ozone-circulation feedback and its implications for global warming
1764 assessments. *Nat Clim Change* 5, 41-45.

1765 Nunes, F., Norris, R.D., 2006. Abrupt reversal in ocean overturning during the Palaeocene/Eocene
1766 warm period. *Nature* 439, 60-63.

1767 O'Brien, C.L., Robinson, S.A., Pancost, R.D., Damste, J.S.S., Schouten, S., Lunt, D.J., Alsenz, H.,
1768 Bomemann, A., Bottini, C., Brassell, S.C., Farnsworth, A., Forster, A., Huber, B.T., Inglis, G.N., Jenkyns,
1769 H.C., Linnert, C., Littler, K., Markwick, P., McAnena, A., Mutterlose, J., Naafs, B.D.A., Puttmann, W.,
1770 Sluijs, A., van Helmond, N.A.G.M., Vellekoop, J., Wagner, T., Wrobel, N.E., 2017. Cretaceous sea-
1771 surface temperature evolution: Constraints from TEX86 and planktonic foraminiferal oxygen
1772 isotopes. *0012-8252* 172, 224-247.

1773 [Outten, S., Esau, I., Ottera, O.H., 2018. Bjerknes Compensation in the CMIP5 Climate Models. *J. Clim.*](#)
1774 [31, 8745-8760.](#)

1775 Pope, V.D., Gallani, M.L., Rowntree, P.R., Stratton, R.A., 2000. The impact of new physical
1776 parametrizations in the Hadley Centre climate model: HadAM3. *Clim. Dyn.* 16, 123-146.

1777 Poulsen, C.J., Barron, E.J., Arthur, M.A., Peterson, W.H., 2001. Response of the mid-Cretaceous
1778 global oceanic circulation to tectonic and CO₂ forcings. *Paleoceanography* 16, 576-592.

1779 Sagoo, N., Valdes, P., Flecker, R., Gregoire, L.J., 2013. The Early Eocene equable climate problem: can
1780 perturbations of climate model parameters identify possible solutions? *Philos T R Soc A* 371.

1781 Scotese, C.R., 2016. PALEOMAP PaleoAtlas for GPlates and the PaleoData Plotter Program,
1782 PALEOMAP Project, <http://www.earthbyte.org/paleomap-paleoatlas-for-gplates/>.

1783 Scotese, C.R., Schettino, A., 2017. Late Permian – Early Jurassic Paleogeography of Western Tethys
1784 and the World, in: Soto, J.I., Flinch, J., Tari, G. (Eds.), *Permo-Triassic Salt Provinces of Europe, North*
1785 *Africa and the Atlantic Margins*. Elsevier, pp. 57-95.

1786 Scotese, C.R., Wright, N., 2018. PALEOMAP Paleodigital Elevation MOdels (PaleoDEMS) for the
1787 Phanerozoic, PALEOMAP Project, [https://www.earthbyte.org/paleodem-resource-scotese-and-](https://www.earthbyte.org/paleodem-resource-scotese-and-wright-2018/)
1788 [wright-2018/](https://www.earthbyte.org/paleodem-resource-scotese-and-wright-2018/).

1789 Smith, R.S., Gregory, J.M., Osprey, A., 2008. A description of the FAMOUS (version XDBUA) climate
1790 model and control run. *Geosci Model Dev* 1, 53-68.

1791 Song, H.J., Wignall, P.B., Song, H.Y., Dai, X., Chu, D.L., 2019. Seawater Temperature and Dissolved
1792 Oxygen over the Past 500 Million Years. *J Earth Sci-China* 30, 236-243.

1793 [Steinthorsdottir, M., H. K. Coxall, A. M. de Boer, M. Huber, N. Barbolini, C. D. Bradshaw, N. J. Burls, S.](#)
1794 [J. Feakins, E. Gasson, J. Henderiks, A. Holbourn, S. Kiel, M. J. Kohn, G. Knorr, W. M. Kurschner, C. H.](#)

1827 [Lear, D. Liebrand, D. J. Lunt, T. Mors, P. N. Pearson, M. J. Pound, H. Stoll, C. A. E. Stromberg, 2021.](#)
1828 [The Miocene: the Future of the Past. Paleoceanography and Paleoclimatology. In press.](#)
1829 [Stoll, H.M., Guitian, J., Hernandez-Almeida, I., Mejia, L.M., Phelps, S., Polissar, P., Rosenthal, Y.,](#)
1830 [Zhang, H.R., Ziveri, P., 2019. Upregulation of phytoplankton carbon concentrating mechanisms](#)
1831 [during low CO₂ glacial periods and implications for the phytoplankton pCO₂ proxy. Quat. Sci. Rev.](#)
1832 [208, 1-20.](#)
1833 Sutton, R.T., Dong, B.W., Gregory, J.M., 2007. Land/sea warming ratio in response to climate change:
1834 IPCC AR4 model results and comparison with observations. Geophys. Res. Lett. 34.
1835 [Upchurch, G.R., Kiehl, J., Shields, C., Scherer, J., Scotese, C., 2015. Latitudinal temperature gradients](#)
1836 [and high-latitude temperatures during the latest Cretaceous: Congruence of geologic data and](#)
1837 [climate models. Geology 43, 683-686.](#)
1838 **Valdes, P.J.**, Armstrong, E., Badger, M.P.S., Bradshaw, C.D., Bragg, F., Crucifix, M., Davies-Barnard, T.,
1839 Day, J.J., Farnsworth, A., Gordon, C., Hopcroft, P.O., Kennedy, A.T., Lord, N.S., Lunt, D.J., Marzocchi,
1840 A., Parry, L.M., Pope, V., Roberts, W.H.G., Stone, E.J., Tourte, G.J.L., Williams, J.H.T., 2017. The
1841 BRIDGE HadCM3 family of climate models: HadCM3@Bristol v1.0. Geosci Model Dev 10, 3715-3743.
1842 Verard, C., Hochard, C., Baumgartner, P.O., Stampfli, G.M., 2015. 3D palaeogeographic
1843 reconstructions of the Phanerozoic versus sea-level and Sr-ratio variations. J Palaeogeog-English 4,
1844 64-84.
1845 Witkowski, C.R., Weijers, J.W.H., Blais, B., Schouten, S., Damste, J.S.S., 2018. Molecular fossils from
1846 phytoplankton reveal secular Pco₂ trend over the Phanerozoic. Sci Adv 4.
1847 You, Y., Huber, M., Muller, R.D., Poulsen, C.J., Ribbe, J., 2009. Simulation of the Middle Miocene
1848 Climate Optimum. Geophys. Res. Lett. 36.
1849 Zachos, J., Pagani, M., Sloan, L., Thomas, E., Billups, K., 2001. Trends, rhythms, and aberrations in
1850 global climate 65 Ma to present. Science 292, 686-693.
1851 Zachos, J.C., Dickens, G.R., Zeebe, R.E., 2008. An early Cenozoic perspective on greenhouse warming
1852 and carbon-cycle dynamics. Nature 451, 279-283.
1853 [Zhou, J., Poulsen, C.J., Pollard, D., White, T.S., 2008. Simulation of modern and middle Cretaceous](#)
1854 [marine delta O-18 with an ocean-atmosphere general circulation model. Paleoceanography 23, 11.](#)
1855 Zhu, J., Poulsen, C.J., Tierney, J.E., 2019. Simulation of Eocene extreme warmth and high climate
1856 sensitivity through cloud feedbacks. Sci Adv 5.

1857

1858

Formate

Table I. List of Paleogeographic Maps and PaleoDEMs

Map Number	Stratigraphic Age Description	Plate Model Age
1	Present-day (Holocene, 0 Ma)	0
2	<i>Last Glacial Maximum (Pleistocene, 21 ky)*</i>	0
3	<i>Late Pleistocene (122 ky)*</i>	0
4	<i>Middle Pleistocene (454 ky)*</i>	0
5	<i>Early Pleistocene (Calabrian, 1.29 Ma)*</i>	0
6	<i>Early Pleistocene (Gelasian, 2.19)*</i>	0
7	Late Pliocene (Piacenzian, 3.09)	5
8	<i>Early Pliocene (Zanclean, 4.47 Ma)*</i>	5
9	<i>latest Miocene (Messinian, 6.3 Ma)*</i>	5
10	Middle/Late Miocene (Serravallian&Tortonian, 10.5 Ma)	10
11	Middle Miocene (Langhian, 14.9 Ma)	15
12	Early Miocene (Aquitania&Burdigalian, 19.5 Ma)	20
13	Late Oligocene (Chattian, 25.6 Ma)	25
14	Early Oligocene (Rupelian, 31 Ma)	30
15	Late Eocene (Priabonian, 35.9 Ma)	35
16	late Middle Eocene (Bartonian, 39.5 Ma)	40
17	early Middle Eocene (Lutetian, 44.5 Ma)	45
18	Early Eocene (Ypresian, 51.9 Ma)	50
19	Paleocene/Eocene Boundary (PETM, 56 Ma)	55
20	Paleocene (Danian&Thanetian, 61 Ma)	60
21	KT Boundary (latest Maastrichtian, 66 Ma)	65
22	Late Cretaceous (Maastrichtian, 69 Ma)	70
23	Late Cretaceous (Late Campanian, 75 Ma)	75
24	Late Cretaceous (Early Campanian, 80.8 Ma)	80
25	Late Cretaceous (Santonian&Coniacian, 86.7 Ma)	85
26	Mid-Cretaceous (Turonian , 91.9 Ma)	90

27	Mid-Cretaceous (Cenomanian, 97.2 Ma)	95
28	Early Cretaceous (late Albian, 102.6 Ma)	100
29	Early Cretaceous (middle Albian, 107 Ma)	105
30	Early Cretaceous (early Albian, 111 Ma)	110
31	Early Cretaceous (late Aptian, 115.8 Ma)	115
32	Early Cretaceous (early Aptian, 121.8 Ma)	120
33	Early Cretaceous (Barremian, 127.2 Ma)	125
34	Early Cretaceous (Hauterivian, 131.2 Ma)	130
35	Early Cretaceous (Valanginian, 136.4 Ma)	135
36	Early Cretaceous (Berriasian, 142.4 Ma)	140
37	Jurassic/Cretaceous Boundary (145 Ma)	145
38	Late Jurassic (Tithonian, 148.6 Ma)	150
39	Late Jurassic (Kimmeridgian, 154.7 Ma)	155
40	Late Jurassic (Oxfordian, 160.4 Ma)	160
41	Middle Jurassic (Callovian, 164.8 Ma)	165
42	Middle Jurassic (Bajocian&Bathonian, 168.2)	170
43	Middle Jurassic (Aalenian, 172.2 Ma)	175
44	Early Jurassic (Toarcian, 178.4 Ma)	180
45	Early Jurassic (Pliensbachian, 186.8 Ma)	185
46	Early Jurassic (Sinemurian/Pliensbachian, 190.8 Ma)	190
47	Early Jurassic (Hettangian&Sinemurian, 196 Ma)	195
48	Late Triassic (Rhaetian/Hettangian, 201.3 Ma)	200
49	Late Triassic (Rhaetian, 204.9 Ma)	205
50	Late Triassic (late Norian, 213.2 Ma)	210
51	Late Triassic (mid Norian, 217.8 Ma)	215
52	Late Triassic (early Norian, 222.4 Ma)	220
53	Late Triassic (Carnian/Norian 227 Ma)	225
54	Late Triassic (Carnian, 232 Ma)	230

55	Late Triassic (early Carnian, 233.6)	235
56	Middle Triassic (Ladinian, 239.5 Ma)	240
57	Middle Triassic (Anisian, 244.6 Ma)	245
58	Permo-Triassic Boundary (252 Ma)	250
59	Late Permian (Lopingian, 256 Ma)	255
60	late Middle Permian (Capitanian, 262.5 Ma)	260
61	Middle Permian (Wordian/Capitanian Boundary 265.1 Ma)	265
62	Middle Permian (Roadian&Wordian, 268.7 Ma)	270
63	Early Permian (late Kungurian, 275 Ma)	275
64	Early Permian (early Kungurian, 280 Ma)	280
65	Early Permian (Artinskian, 286.8 Ma)	285
66	Early Permian (Sakmarian, 292.6 Ma)	290
67	Early Permian (Asselian, 297 Ma)	295
68	Late Pennsylvanian (Gzhelian, 301.3 Ma)	300
69	Late Pennsylvanian (Kasimovian, 305.4 Ma)	305
70	Middle Pennsylvanian (Moscovian, 311.1 Ma)	310
	Early/Middle Carboniferous (Baskirian/Moscovian	
71	boundary, 314.6 Ma)	315
72	Early Pennsylvanian (Bashkirian, 319.2 Ma)	320
73	Late Mississippian (Serpukhovian, 327 Ma)	325
	Late Mississippian (Visean/Serpukhovian boundary, 330.9	
74	Ma)	330
75	Middle Mississippian (late Visean, 333 Ma)	335
76	Middle Mississippian (middle Visean, 338.8Ma)	340
77	Middle Mississippian (early Visean, 344 Ma)	345
78	Early Mississippian (late Tournaisian, 349 Ma)	350
79	Early Mississippian (early Tournaisian, 354Ma)	355
80	Devono-Carboniferous Boundary (358.9 Ma)	360
81	Late Devonian (middle Famennian, 365.6 Ma)	365

82	Late Devonian (early Famennian, 370 Ma)	370
83	Late Devonian (late Frasnian, 375 Ma)	375
84	Late Devonian (early Frasnian, 380 Ma)	380
85	Middle Devonian (Givetian, 385.2 Ma)	385
86	Middle Devonian (Eifelian, 390.5 Ma)	390
87	Early Devonian (late Emsian, 395 Ma)	395
88	Early Devonian (middle Emsian, 400 Ma)	400
89	Early Devonian (early Emsian, 405 Ma)	405
90	Early Devonian (Pragian, 409.2 Ma)	410
91	Early Devonian (Lochkovian, 415 Ma)	415
92	Late Silurian (Pridoli, 421.1 Ma)	420
93	Late Silurian (Ludlow, 425.2 Ma)	425
94	Middle Silurian (Wenlock, 430.4 Ma)	430
95	Early Silurian (late Llandovery, 436 Ma)	435
96	Early Silurian (early Llandovery, 441.2 Ma)	440
97	Late Ordovician (Hirnantian, 444.5 Ma)	445
98	Late Ordovician (Katian, 449.1 Ma)	450
99	Late Ordovician (Sandbian, 455.7 Ma)	455
100	Middle Ordovician (late Darwillian, 460 Ma)	460
101	Middle Ordovician (early Darwillian, 465 Ma)	465
102	Early Ordovician (Floian/Dapingian boundary, 470 Ma)	470
103	Early Ordovician (late Early Floian, 475 Ma)	475
104	Early Ordovician (Tremadoc, 481.6 Ma)	480
105	Cambro-Ordovician Boundary (485.4 Ma)	485
106	Late Cambrian (Jiangshanian, 491.8 Ma)	490
107	Late Cambrian (Pabian, 495.5 Ma)	495
108	late Middle Cambrian (Guzhangian, 498.8 Ma)	500
109	late Middle Cambrian (early Epoch 3, 505 Ma)	505

110	early Middle Cambrian (late Epoch 2, 510 Ma)	510
111	early Middle Cambrian (middle Epoch 2, 515 Ma)	515
112	Early/Middle Cambrian boundary (520 Ma)	520
113	Early Cambrian (late Terreneuvian, 525 Ma)	525
114	Early Cambrian (middle Terreneuvian, 530 Ma)	530
115	Early Cambrian (early Terreneuvian, 535 Ma)	535
116	Cambrian/Precambrian boundary (541 Ma)	540

1859 * *Simulations were not run for the time intervals highlighted in italics.*

1860

1861